

---

# ProjMC<sup>2</sup>: Scalable and Stable Posterior Inference for Bayesian Spatial Factor Models with Application to Spatial Transcriptomics

LU ZHANG

USC PPHS DIVISION OF BIOSTATISTICS

lzhang63@usc.edu

June 3, 2025

## Abstract

*Factor models exhibit a fundamental tradeoff among flexibility, identifiability, and computational efficiency. Bayesian spatial factor models, in particular, face pronounced identifiability concerns and scaling difficulties. To mitigate these issues and enhance posterior inference reliability, this work proposes Projected Markov Chain Monte Carlo (ProjMC<sup>2</sup>), a novel Markov Chain Monte Carlo (MCMC) sampling algorithm employing projection techniques and conditional conjugacy. ProjMC<sup>2</sup> is showcased within the context of spatial factor analysis, significantly improving posterior stability and MCMC mixing efficiency by projecting posterior sampling of latent factors onto a subspace of a scaled Stiefel manifold. Theoretical results establish convergence to the stationary distribution irrespective of initial values. Integrating this approach with scalable univariate spatial modeling strategies yields a stable, efficient, and flexible modeling and sampling methodology for large-scale spatial factor models. Simulation studies demonstrate the effectiveness and practical advantages of the proposed methods. The practical utility of the methodology is further illustrated through an analysis of spatial transcriptomic data obtained from human kidney tissues, showcasing its potential for enhancing the interpretability and robustness of spatial transcriptomics analyses.*

**Key words:** Factor Analysis; Multivariate Spatial Modeling; High-Dimensional Spatial Data; Gaussian Process; Identifiability

---

## 1. INTRODUCTION

Multivariate geo-indexed datasets are increasingly prevalent across disciplines, including environmental science, genomics, public health, ecology, economics, and urban studies. These datasets measure multiple variables across shared spatial domains, often exhibiting spatial autocorrelation—where nearby locations have similar values—and spatial cross-correlation—where variables demonstrate spatial interdependencies (Banerjee et al., 2014; Cressie and Wike, 2015). Such correlations typically reflect geographic proximity and common underlying drivers. Analyzing these joint spatial patterns helps reveal latent dependencies and potential causal mechanisms. For instance, spatial omics involves quantifying various molecular measurements (e.g., gene expression, protein abundances, metabolites) within biological tissues, where patterns reflect the spatially structured biological microenvironment (Moses and Pachter, 2022; Bressan et al., 2023; Lee et al., 2025). Identifying spatially correlated molecular signatures can enhance understanding of tissue heterogeneity. Similarly, multivariate pollutant data in environmental science can indicate diverse sources, such as vehicular emissions or industrial discharge (Song et al., 2018; Dai et al., 2024). Uncovering these latent spatial structures is crucial for source identification and risk assessment.

Spatial factor analysis offers a valuable framework for exploring underlying spatially correlated factors within multivariate datasets. Analogous to classical latent factor analysis (FA), spatial factor models represent a latent multivariate spatial process as a linear combination of a small number of common spatially correlated factors. The foundational concepts and subsequent elaborations of spatial factor models have been explored in key works by Wang and Wall (2003), Lopes et al. (2008) and Velten et al. (2022). Despite their established utility, a significant challenge in applying spatial factor models, especially those employing Gaussian Process (GP) distributions for the spatial factors, is their computational burden. The computational costs and storage requirements scale cubically and quadratically, respectively, with the number of spatial locations  $n$ , rendering them impractical for large-scale datasets (Stein, 1999; Banerjee et al., 2014; Cressie and Wike, 2015). To mitigate this scalability bottleneck, several approaches have focused on low-rank approximations of the spatial factors. These include methods based on Predictive Processes (Banerjee et al., 2008; Finley et al., 2009) or Inducing points (Titsias, 2009), as explored in studies by Ren and Banerjee (2013), Shang and Zhou (2022), and Townes and Engelhardt (2023). Nevertheless, such approaches that employ a reduced rank representation of the desired spatial process cannot scale to modest large datasets (with tens of thousands of locations) and can result in over-smoothing the latent process from massive data sets (Stein, 2014).

More recently, the use of Nearest-Neighbor Gaussian Processes (NNGP) (Datta et al., 2016), which fall under the broader class of Vecchia approximations for scalable GP (see, e.g. Katzfuss and Guinness, 2021),

---

have emerged as a promising alternative for modeling spatial factors, gaining traction in recent literature (Taylor-Rodriguez et al., 2019; Zhang and Banerjee, 2022). NNGPs offer a scalable approximation to full GPs that can capture both global and local spatial pattern for large datasets (Zhang et al., 2024). However, while Zhang and Banerjee (2022) emphasize predictive performance, their work does not fully address the critical issue of parameter identifiability, which is essential for recovering underlying spatial patterns. In contrast, Taylor-Rodriguez et al. (2019) adopt constraints common in non-spatial factor analysis to achieve identifiability, which is unnecessarily stringent as argued in Ren and Banerjee (2013). Furthermore, a critical gap persists in the literature, including Ren and Banerjee (2013) and Taylor-Rodriguez et al. (2019), concerning the practical implications of weak identifiability. Specifically, the impact of identifiability issues related to intercept terms and GP hyperparameters (challenges well-documented in the general GP literature, e.g., Stein (1999), Zhang (2004), Zhang and Zimmerman (2005), Du et al. (2009), Tang et al. (2021)) on the implementation and posterior sampling efficiency of spatial factor models remains largely unaddressed.

This paper introduces a novel Bayesian spatial factor model designed for scalability with large spatial datasets, while concurrently imposing minimal, yet effective, restrictions to mitigate the slow convergence and poor mixing engendered by the inherent identifiability issues in factor models. The core of this work is a novel model construction and sampling algorithm, termed Projected Markov Chain Monte Carlo (ProjMC<sup>2</sup>). Specifically, within a blocked Gibbs sampling framework for a spatial factor model, a projection step is introduced to project the high-dimensional factor realizations to a subspace of the Stiefel manifold (Chakraborty and Vemuri, 2019), thereby enhancing identifiability and substantially improving sampling efficiency for parameters that suffer from weak or non-identifiability. Theoretical results establishing the existence, convergence, and properties of the posterior distribution induced by the ProjMC<sup>2</sup> algorithm are presented in Section 3. The efficacy of the ProjMC<sup>2</sup> algorithm is demonstrated within the context of a scalable spatial factor model where the spatially varying factors are modeled using NNGPs. A detailed implementation algorithm is provided in Section 4.1. It is noteworthy that while the primary contributions—ProjMC<sup>2</sup> and its application to scalable spatial factor model—are presented in tandem, the foundational concept of ProjMC<sup>2</sup>, which constructs the model via conditional distributions and transition kernels, is generalizable to a broader class of factor models.

To illustrate the practical utility and advantages of the proposed Bayesian spatial factor model, this work features an application to a spatial transcriptomics dataset derived from human kidney tissue. Section 6 presents a comparative analysis against contemporary ‘black-box’ auto-encoder-based algorithms, STAGATE (Dong and Zhang, 2022) and GraphST (Long et al., 2023), specifically for the task of spatial domain identification. The results demonstrate that the proposed methodology achieves performance comparable

to, and in some instances superior to, these leading competitors. More critically, it yields more interpretable insights into the underlying complex biological systems, an advantage of particular significance when analyzing novel spatial omics data that lack pre-existing annotations or labels. Consequently, the proposed methodology provides a scalable, fully Bayesian, probability-based regression framework for large-scale spatial omics data. This framework matches the representational capacity of current auto-encoder-based approaches while distinctly offering enhanced interpretability and uncertainty quantification.

The remainder is organized as follows. Section 2 introduces notation and provides background on Bayesian spatial factor models. Section 5 presents simulation studies evaluating the performance of the proposed methodology, including a comprehensive sensitivity analysis to investigate the influence of different algorithmic choices on the mixing of weakly identifiable parameters and to assess the practical behavior of the proposed methodology. Finally, Section 7 offers concluding remarks and discusses avenues for future research.

## 2. BAYESIAN SPATIAL FACTOR MODEL AND SAMPLING

**Bayesian Spatial Factor (BSF) Model:** Let  $\mathbf{y}(\mathbf{s}) = (y_1(\mathbf{s}), \dots, y_q(\mathbf{s}))^\top \in \mathbb{R}^q$  denote the  $q \times 1$  vector of dependent outcomes in location  $\mathbf{s} \in \mathcal{D} \subset \mathbb{R}^d$ ,  $\mathbf{x}(\mathbf{s}) = (x_1(\mathbf{s}), \dots, x_p(\mathbf{s}))^\top \in \mathbb{R}^p$  be the corresponding explanatory variables, and  $\boldsymbol{\beta}$  be a  $p \times q$  regression coefficient matrix. A factor model can be denoted as

$$\mathbf{y}(\mathbf{s}) = \boldsymbol{\beta}^\top \mathbf{x}(\mathbf{s}) + \boldsymbol{\Lambda}^\top \mathbf{f}(\mathbf{s}) + \boldsymbol{\epsilon}(\mathbf{s}), \mathbf{s} \in \mathcal{D}, \quad (2.1)$$

where  $\boldsymbol{\Lambda}$  is a  $K \times q$  loading matrix and  $\mathbf{f}(\mathbf{s}) = (f_1(\mathbf{s}), \dots, f_K(\mathbf{s}))'$  denotes a vector of  $K$  components. Each component  $f_k(\mathbf{s})$  represents the  $k$ -th factor's realization at location  $\mathbf{s}$ .  $\boldsymbol{\lambda}_k^\top$  is the  $k$ -th row of  $\boldsymbol{\Lambda}$ . The noise process  $\boldsymbol{\epsilon}(\mathbf{s}) \stackrel{iid}{\sim} \mathbf{N}(\mathbf{0}, \boldsymbol{\Sigma})$  with covariance matrix  $\boldsymbol{\Sigma}$ . When assigning the factors  $\mathbf{f}(\mathbf{s})$  with a prior with belief in spatial correlation or spatial pattern, the hierarchical model (2.1) is referred to as a spatial factor model. Typical choices of such priors include Gaussian processes (GPs). Here, it is further assumed that each factor  $f_k(\mathbf{s})$  independently follows a GP with correlation function  $\rho_{\psi_k}(\cdot, \cdot)$  with hyperparameters  $\psi_k$ , i.e.,

$$f_k(\mathbf{s}) \sim \text{GP}(0, \rho_{\psi_k}(\cdot, \cdot)), k = 1, \dots, K. \quad (2.2)$$

As illustrated in Zhang and Banerjee (2022), a convenient choice for the priors of parameters  $\{\boldsymbol{\beta}, \boldsymbol{\Lambda}, \boldsymbol{\Sigma}\}$  in the spatial factor model is the Matrix-Normal-Inverse-Wishart(MNIW) family,

$$\boldsymbol{\beta} \mid \boldsymbol{\Sigma} \sim \text{MN}(\boldsymbol{\mu}_\beta, \mathbf{V}_\beta, \boldsymbol{\Sigma}); \boldsymbol{\Lambda} \mid \boldsymbol{\Sigma} \sim \text{MN}(\boldsymbol{\mu}_\Lambda, \mathbf{V}_\Lambda, \boldsymbol{\Sigma}); \boldsymbol{\Sigma} \sim \text{IW}(\boldsymbol{\Psi}, \nu) \quad , \quad (2.3)$$



where  $\text{MN}_{n,p}(\mathbf{M}, \mathbf{U}, \mathbf{V})$  denotes a Matrix-Normal distribution (Dawid, 1981) with mean matrix  $\mathbf{M}$ , the first  $n \times n$  scale matrix  $\mathbf{U}$ , and the second  $p \times p$  scale matrix  $\mathbf{V}$ ,  $\boldsymbol{\mu}_\Lambda$  is a  $q \times K$  matrix and  $\mathbf{V}_\Lambda$  is a  $K \times K$  positive definite matrix. The model defined by (2.1)–(2.3) is referred to as the Bayesian spatial factor (BSF) model. This model can be readily adapted for spatial data with misalignment, and for a more general formulation, see Zhang and Banerjee (2022). Given that the present application involves spatial transcriptomic data, the focus here is on the scenario where there is no missing outcome across different locations.

Without misalignment, model in (2.1) can be cast as  $\mathbf{Y}_{n \times q} = \mathbf{X}_{n \times p} \boldsymbol{\beta}_{p \times q} + \mathbf{F}_{n \times K} \boldsymbol{\Lambda}_{K \times q} + \boldsymbol{\epsilon}_{n \times q}$ , where  $\mathbf{Y} = \mathbf{y}(S) = [\mathbf{y}(\mathbf{s}_1) : \dots : \mathbf{y}(\mathbf{s}_n)]^\top$  is the  $n \times q$  response matrix,  $\mathbf{X} = \mathbf{x}(S) = [\mathbf{x}(\mathbf{s}_1) : \dots : \mathbf{x}(\mathbf{s}_n)]^\top$  is the design matrix with full rank ( $n > p$ ), and  $\mathbf{F}$  is the  $n \times K$  matrix with  $j$ -th column being the  $n \times 1$  vector comprising  $f_j(\mathbf{s}_i)$ 's for  $i = 1, 2, \dots, n$ . Define  $\boldsymbol{\rho}_{\psi_k}(S, S)$  to be the  $n \times n$  spatial correlation matrix for  $\mathbf{f}_k = (f_k(\mathbf{s}_1), f_k(\mathbf{s}_2), \dots, f_k(\mathbf{s}_n))^\top$ . Denote matrix vectorization by stacking its columns, i.e.,  $\text{vec}(\mathbf{F}) = (f_1(\mathbf{s}_1), \dots, f_1(\mathbf{s}_n), \dots, f_K(\mathbf{s}_1), \dots, f_K(\mathbf{s}_n))^\top$ , we have  $\text{vec}(\mathbf{F}) \sim \text{N}(\mathbf{0}, \oplus_{k=1}^K \{\boldsymbol{\rho}_{\psi_k}(S, S)\})$ , and  $\oplus_{i=1}^n$  represents the block diagonal operator stacking matrices along the diagonal.

**Conditional Posterior of BSF Model and Posterior Sampling:** The BSF model yields conjugate conditional posteriors, enabling an efficient Gibbs sampling with block updates. When  $\mathbf{F}$  is fixed, under the MNIW prior (2.3) on  $\{\boldsymbol{\beta}, \boldsymbol{\Lambda}, \boldsymbol{\Sigma}\}$ , the posterior for  $\boldsymbol{\gamma} = [\boldsymbol{\beta}^\top, \boldsymbol{\Lambda}^\top]^\top$  and  $\boldsymbol{\Sigma}$  remains in the MNIW family. Specifically,

$$(\boldsymbol{\gamma}, \boldsymbol{\Sigma}) \mid (\mathbf{F}, \mathbf{Y}) \sim \text{MNIW}(\boldsymbol{\mu}^*, \mathbf{V}^*, \boldsymbol{\Psi}^*, \nu^*), \quad (2.4)$$

where  $\mathbf{V}^* = [\mathbf{X}^{*\top} \mathbf{X}^*]^{-1}$ ,  $\boldsymbol{\mu}^* = \mathbf{V}^* [\mathbf{X}^{*\top} \mathbf{Y}^*]$ ,  $\boldsymbol{\Psi}^* = \boldsymbol{\Psi} + \mathbf{S}^*$ ,  $\nu^* = \nu + n$ , and  $\mathbf{S}^* = (\mathbf{Y}^* - \mathbf{X}^* \boldsymbol{\mu}^*)^\top (\mathbf{Y}^* - \mathbf{X}^* \boldsymbol{\mu}^*)$ . Here  $\mathbf{X}^*$  and  $\mathbf{Y}^*$  arise from the augmented linear system

$$\underbrace{\begin{bmatrix} \mathbf{Y} \\ \mathbf{L}_\beta^{-1} \boldsymbol{\mu}_\beta \\ \mathbf{L}_\Lambda^{-1} \boldsymbol{\mu}_\Lambda \end{bmatrix}}_{\mathbf{Y}^*} = \underbrace{\begin{bmatrix} \mathbf{X} & \mathbf{F} \\ \mathbf{L}_\beta^{-1} & \mathbf{0} \\ \mathbf{0} & \mathbf{L}_\Lambda^{-1} \end{bmatrix}}_{\mathbf{X}^*} \underbrace{\begin{bmatrix} \boldsymbol{\beta} \\ \boldsymbol{\Lambda} \end{bmatrix}}_{\boldsymbol{\gamma}} + \underbrace{\begin{bmatrix} \boldsymbol{\eta}_1 \\ \boldsymbol{\eta}_2 \\ \boldsymbol{\eta}_3 \end{bmatrix}}_{\boldsymbol{\eta}^*}, \quad (2.5)$$

where  $\mathbf{V}_\Lambda = \mathbf{L}_\Lambda \mathbf{L}_\Lambda^\top$ , and  $\boldsymbol{\eta}^* \sim \text{MN}(\mathbf{0}_{(n+p+K) \times q}, \mathbf{I}_{n+p+K}, \boldsymbol{\Sigma})$ . Next, suppose  $\{\boldsymbol{\beta}, \boldsymbol{\Lambda}, \boldsymbol{\Sigma}\}$  are given and  $\{\psi_k\}_{k=1}^K$  are prefixed. Let  $\boldsymbol{\rho}_{\psi_k}(S, S) = \mathbf{L}_k \mathbf{L}_k^\top$  for each  $k$ ,

$$\text{vec}(\mathbf{F}) \mid (\boldsymbol{\gamma}, \boldsymbol{\Sigma}, \mathbf{Y}) \sim \text{N}((\tilde{\mathbf{X}}^\top \tilde{\mathbf{X}})^{-1} \tilde{\mathbf{X}}^\top \tilde{\mathbf{Y}}, (\tilde{\mathbf{X}}^\top \tilde{\mathbf{X}})^{-1}), \quad (2.6)$$

where  $\tilde{\mathbf{Y}} = [\text{vec}((\mathbf{Y} - \mathbf{X}\boldsymbol{\beta})\boldsymbol{\Sigma}^{-1/2})^\top, \mathbf{0}_{n \times K}^\top]^\top$  and  $\tilde{\mathbf{X}} = [(\boldsymbol{\Lambda} * \boldsymbol{\Sigma}^{-1/2}) \otimes \mathbf{I}_n : \oplus_{k=1}^K \mathbf{L}_k^{-\top}]^\top$ . These conjugate conditional distributions naturally lend themselves to a blocked Gibbs sampler.

---

**Non-identifiability issue:** Although the blocked Gibbs sampler performs well for interpolation and prediction tasks as shown in Zhang and Banerjee (2022), it is not efficient for factor analysis due to inherent non-identifiability issues. The non-identifiability problem arises firstly from the construction  $\Lambda^\top \mathbf{f}(\mathbf{s})$  in the target factor model (2.1), where scaling and permuting rows of  $\Lambda$  and the corresponding elements in  $\mathbf{f}(\mathbf{s})$  can yield the same likelihood. This degeneracy persists regardless of sample size. In practise, this will cause poor convergence and mixing of the Markov chain Monte Carlo (MCMC) chains for  $\Lambda$  and  $\mathbf{f}(\mathbf{s})$ , though the MCMC chain for the product  $\Lambda^\top \mathbf{f}(\mathbf{s})$  may converge faster. Additionally, since only samples for  $\Lambda^\top \mathbf{f}(\mathbf{s})$  are reliable, we need to recover the posterior samples of  $\Lambda^\top \mathbf{f}(\mathbf{s})$ . When  $q$  is large and  $k$  is small, the storage of the sample for  $\Lambda^\top \mathbf{f}(\mathbf{s})$  can be expensive. Moreover, spatial factors  $\mathbf{f}(\mathbf{s})$  and the intercepts for each outcome may not be identifiable from one another (Stein, 1999), further complicating inference. When each factor is modeled via a Gaussian process with a Matérn covariance function (Matérn, 1986), additional non-identifiability arises among the hyperparameters (Zhang, 2004; Zhang and Zimmerman, 2005; Du et al., 2009; Tang et al., 2021). Consequently, the block-update approach converges slowly and exhibits mixing difficulties for posterior inference in factor analysis settings.

### 3. PROJECTED MARKOV CHAIN MONTE CARLO

This section introduces a Projected Markov Chain Monte Carlo (ProjMC<sup>2</sup>) algorithm specifically tailored to the Bayesian Spatial Factor (BSF) model. The core motivation is to improve sampling efficiency for factor analysis by reducing redundant or non-identifiable directions within the latent factor space. Though presented in the BSF model context, the underlying theorems can be extended to broader hierarchical settings where similar latent variable identifiability issues occur.

#### 3.1. ProjMC<sup>2</sup> sampling for BSF Model

Let  $\mathbf{F} \in \mathbb{R}^{n \times K}$  denote the latent factor matrix in the BSF model, as introduced in Section 2. Define the projection

$$g: \mathbb{R}^{n \times K} \rightarrow \Omega^g, \quad \mathbf{F} = [\mathbf{f}_1 : \dots : \mathbf{f}_K] \mapsto \tilde{\mathbf{F}} = \sqrt{n} \text{QR}\{(I_n - \frac{1}{n} \mathbf{1}_n \mathbf{1}_n^\top) \mathbf{F}\}, \quad (3.1)$$

where  $\text{QR}\{A\}$  produces the  $Q$ -factor of the thin QR decomposition of a matrix  $A$ ,  $\mathbf{1}_n$  is the  $n$ -dimensional vector of all ones,  $I_n$  is the  $n \times n$  identity matrix, and  $\Omega^g \subset \mathbb{R}^{n \times K}$  denote the image (range) of  $g(\cdot)$ . This map  $g(\mathbf{F})$  first *centers* the columns of  $\mathbf{F}$  (by subtracting their sample means) and then *projects* the centered

matrix onto a scaled Stiefel manifold Chakraborty and Vemuri (2019). Its inverse set is given by

$$g^{-1}(\tilde{\mathbf{F}}) = \{\mathbf{F} : g(\mathbf{F}) = \tilde{\mathbf{F}}\} = \{\tilde{\mathbf{F}} R + \mathbf{1}_n \mu_f^\top \mid R \in U_K^+, \mu_f \in \mathbb{R}^K\}, \quad (3.2)$$

where  $U_K^+$  is the space of  $K \times K$  upper-triangular matrices with positive diagonal entries. Let  $\mathcal{L}^{n \times K}$  be the Lebesgue measure on  $\mathbb{R}^{n \times K}$ . We write  $\varphi = \mathcal{L}^{n \times K} \circ g^{-1}$  for the induced (pushforward) measure of  $\mathcal{L}^{n \times K}$  onto  $\Omega^g$ .

With this projection in place, a Markov chain Monte Carlo procedure is constructed based on block Gibbs updates for the BSF model. A simplified flowchart is shown in Figure 1. The projected MCMC forces the

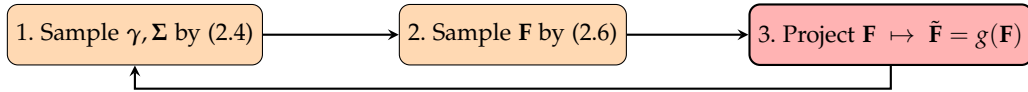


Figure 1: Simplified flowchart of the projected MCMC algorithm.

sampling space of  $\{\mathbf{F}, \gamma, \Sigma\}$  on  $\Omega^g \times \mathbb{R}^{(p+K) \times q} \times \mathbb{S}_+^q$ , where  $\mathbb{S}_+^q$  is the space of  $q \times q$  symmetric positive-definite (SPD) matrices. Define  $\Psi$  as the pushforward of the product measure  $\mathcal{L}^{n \times K} \times \mathcal{L}^{(p+K) \times q} \times \nu_{\mathbb{S}_+^q}$  through the map  $(\mathbf{F}, \gamma, \Sigma) \mapsto (g(\mathbf{F}), \gamma, \Sigma)$ , where  $\nu_{\mathbb{S}_+^q}$  is a base measure (often taken as a standard Riemannian measure) on  $\mathbb{S}_+^q$ . Equivalently, one may write  $\Psi = \varphi \times \mathcal{L}^{(p+K) \times q} \times \nu_{\mathbb{S}_+^q}$ .

A quantitative description of the sampling process follows. Suppose there are current draws  $\{\tilde{\mathbf{F}}^{(l)}, \gamma^{(l)}, \Sigma^{(l)}\}$  at the  $l$ -th iteration. The steps for iteration  $l+1$  proceed as follows:

- (i) Sample  $(\gamma^{(l+1)}, \Sigma^{(l+1)})$  using the conditional distribution given in (2.4) with  $\mathbf{F} = \tilde{\mathbf{F}}^{(l)}$ .
- (ii) Update  $\tilde{\mathbf{F}}^{(l+1)}$  from the distribution with density

$$p(\tilde{\mathbf{F}}^{(l+1)} \mid \gamma^{(l+1)}, \Sigma^{(l+1)}) = \int_{g^{-1}(\tilde{\mathbf{F}}^{(l+1)})} p(\mathbf{F} \mid \gamma^{(l+1)}, \Sigma^{(l+1)}, \mathbf{Y}) d\mathbf{F},$$

where  $p(\mathbf{F} \mid \gamma^{(l+1)}, \Sigma^{(l+1)}, \mathbf{Y})$  is the density of the conditional posterior distribution in (2.6).

We have the following Lemma.

**Lemma 3.1** (Transition Kernel of ProjMC<sup>2</sup>). *Let  $\theta_1 = \{\tilde{\mathbf{F}}_1, \gamma_1, \Sigma_1\}$ ,  $\theta_2 = \{\tilde{\mathbf{F}}_2, \gamma_2, \Sigma_2\}$  be two points in the sample space  $\Theta := \Omega^g \times \mathbb{R}^{(p+K) \times q} \times \mathbb{S}_{++}^q$ , the transition kernel of the projected MCMC for the BSF model is*

$$K(\theta_1, \theta_2) = \int_{g^{-1}(\tilde{\mathbf{F}}_2)} p(\mathbf{F} \mid \gamma_2, \Sigma_2, \mathbf{Y}) d\mathbf{F} p(\gamma_2, \Sigma_2 \mid \tilde{\mathbf{F}}_1, \mathbf{Y}), \quad (3.3)$$

where densities  $p(\mathbf{F} \mid \gamma, \Sigma, \mathbf{Y})$  and  $p(\gamma, \Sigma \mid \mathbf{F}, \mathbf{Y})$  are given in (2.4) and (2.6), respectively.

*Proof.* In view of step (i) and (ii), we obtain that for any Borel sets  $A_1 \in \mathcal{B}(\Omega^g)$ ,  $A_2 \in \mathcal{B}(\mathbb{R}^{(p+K) \times q})$ ,  $A_3 \in \mathcal{B}(\mathcal{S}_+^q)$ , when  $A = A_1 \times A_2 \times A_3$ , the conditional probability of transiting from  $\theta_1$  to  $A$  is

$$K(\theta_1, A) = \int_{A_2 \times A_3} \left\{ \int_{g^{-1}(A_1)} p(\mathbf{F} \mid \gamma, \Sigma, \mathbf{Y}) d\mathbf{F} \right\} p(\gamma, \Sigma \mid \tilde{\mathbf{F}}_1, \mathbf{Y}) d\gamma d\Sigma.$$

Further, by taking  $A$  to be the whole space,  $\int_{g^{-1}(\Omega^g)} p(\mathbf{F} \mid \gamma^{(l+1)}, \Sigma^{(l+1)}, \mathbf{Y}) d\mathbf{F} = \int_{\mathbb{R}^{n \times K}} p(\mathbf{F} \mid \gamma^{(l+1)}, \Sigma^{(l+1)}, \mathbf{Y}) d\mathbf{F} = 1$ . Hence,  $K(\theta_1, \cdot)$  is a probability measure for any  $\theta_1$ . Meanwhile, for any  $A \in \mathcal{B}(\Theta)$ ,  $K(\cdot, A)$  is continuous, and thus measurable. Through the definition 4.2.1 of transition kernel in Robert et al. (1999), (3.3) is a valid transition kernel.  $\square$

### 3.2. Theoretical Properties of the ProjMC<sup>2</sup> Algorithm

In this subsection, it is formally demonstrated that the Markov chain  $(\theta_l)$  defined by the transition kernel (3.3) admits a unique stationary distribution, and that, for any initial point in its state space, the chain converges to this target density. These results ensure the validity and consistency of our ProjMC<sup>2</sup> approach for Bayesian inference within the proposed factor model.

**Theorem 3.2** (Convergence). *Let  $(\theta_\ell)$  be the Markov chain on  $\Theta$  with transition kernel  $K$  given in (3.3),  $(\theta_\ell)$  converges in total variation to its unique stationary distribution  $\pi(\cdot)$ . Hence, for any initial state  $\theta \in \Theta$ ,*

$$\lim_{l \rightarrow \infty} \|K^l(\theta, \cdot) - \pi(\cdot)\|_{\text{TV}} = 0,$$

where for two probability measures  $\mu_1$  and  $\mu_2$  on  $\Theta$ , the total variation distance is defined as

$$\|\mu_1 - \mu_2\|_{\text{TV}} = \sup_{A \subseteq \Theta} |\mu_1(A) - \mu_2(A)|.$$

*Proof.* By Lemma 3.6, the Markov chain  $(\theta_l)$  is Harris positive. By Lemma 3.4,  $(\theta_l)$  is aperiodic. Then, it follows immediately from (Robert et al., 1999, Theorem 4.6.5) that Theorem 3.2 holds.  $\square$

**Lemma 3.3** (Strong  $\Psi$ -irreducibility). *Let  $(\theta_\ell)$  be the Markov chain on  $\Theta$  with transition kernel  $K$  given in (3.3), and let  $\Psi$  be the measure on  $\Theta$  defined in Section 3.1. For every measurable set  $A \subseteq \Theta$  with  $\Psi(A) > 0$ , we have*

$$K(\theta, A) > 0 \quad \text{for all } \theta \in \Theta.$$

Hence,  $(\theta_\ell)$  is strongly  $\Psi$ -irreducible.

*Proof.* By construction, for each  $\theta = \{\tilde{\mathbf{F}}, \gamma, \Sigma\} \in \Theta$ , the kernel  $K(\theta, \cdot)$  assigns mass to any Borel set  $A$

according to

$$K(\theta, A) = \int_A \left\{ \int_{g^{-1}(\tilde{\mathbf{F}}')} p(\mathbf{F} \mid \gamma', \Sigma', \mathbf{Y}) d\mathbf{F} \right\} p(\gamma', \Sigma' \mid \tilde{\mathbf{F}}, \mathbf{Y}) d\tilde{\mathbf{F}}' d\gamma' d\Sigma'.$$

Since the densities  $p(\mathbf{F} \mid \gamma, \Sigma, \mathbf{Y})$  and  $p(\gamma, \Sigma \mid \mathbf{F}, \mathbf{Y})$  are strictly positive over their supports, for any set  $A$  with  $\Psi(A) > 0$ , it follows that

$$K(\theta, A) = \int_A (\text{positive integrand}) > 0, \quad \forall \theta \in \Theta.$$

By definition (see, e.g., (Robert et al., 1999, Definition 4.3.1)), if  $K(\theta, A) > 0$  for all  $\theta$  whenever  $\Psi(A) > 0$ , the chain is strongly  $\Psi$ -irreducible.  $\square$

**Lemma 3.4** (Aperiodicity). *Under the same conditions as in Lemma 3.3, the Markov chain  $(\theta_\ell)$  is aperiodic.*

*Proof.* Based on Meyn and Tweedie (2012, Thm 5.4.4), an irreducible Markov chain on a general state space  $\Theta$  is said to be  $d$ -cycle with  $d > 1$  if there exists  $d$  disjoint Borel sets  $\{D_0, D_1, \dots, D_{d-1}\}$  such that

- (i)  $K(\theta, D_{(i+1) \bmod d}) = 1$  for all  $\theta \in D_i$ ,  $i = 0, \dots, d-1$ .
- (ii) The set  $N = [\cup_{i=0}^{d-1} D_i]^c$  is  $\Psi$ -null. And  $\Psi(D_i) > 0$  for  $i = 0, \dots, d-1$

Suppose, for contradiction,  $d > 1$ . Pick any  $\theta \in D_i$ . By definition,

$$K(\theta, D_{(i+1) \bmod d}) = 1, \quad \text{meaning} \quad K(\theta, \Theta \setminus D_{(i+1) \bmod d}) = 0.$$

However, under our assumptions (strict positivity of densities and hence full support), for *every*  $\theta \in \Theta$  and *every* nonempty Borel set  $B \subseteq \Theta$ , we have  $K(\theta, B) > 0$ . In particular, if we choose  $B = \Theta \setminus D_{(i+1) \bmod d}$ , then  $\theta \in D_i$  implies  $K(\theta, B) > 0$ . This contradicts  $K(\theta, B) = 0$ . By definition, this implies that  $(\theta_\ell)$  has  $d = 1$  and is thus *aperiodic* (see, e.g. the definition in (Meyn and Tweedie, 2012, Chp 5).  $\square$

According to Definition 4.4.8 in Robert et al. (1999), the chain  $(\theta_\ell)$  is *Harris recurrent* if there exists a measure  $\Psi$  such that

- (i)  $(\theta_\ell)$  is  $\Psi$ -irreducible, and
- (ii) for every set  $A$  with  $\Psi(A) > 0$ ,  $A$  is *Harris recurrent*.

A set  $A$  is *Harris recurrent* if  $P_\theta(\eta_A = \infty) = 1$  for all  $\theta \in A$ , where  $\eta_A$  is the number of passages of  $(\theta_\ell)$  in  $A$  and  $P_\theta(\eta_A = \infty)$  is the probability of visiting  $A$  an infinite number of times starting from the initial point  $\theta_1 = \theta$ .

**Lemma 3.5** (Recurrence). *The chain  $(\theta_l)$  is Harris recurrent.*

*Proof.* Suppose  $A$  is a set with  $\Psi(A) > 0$ . Through the definition of the transition kernel in Lemma 3.1, we observe that  $K(\theta_1, A)$  for  $\theta_1 = \{\tilde{\mathbf{F}}_1, \gamma_1, \Sigma_1\}$  only depends on  $\tilde{\mathbf{F}}_1$ . Since  $\tilde{\mathbf{F}}_1$  belongs to a compact set  $\Omega^g$ , the infimum  $\inf_{\theta} \int_A K(\theta, y) dy = \rho > 0$ . The probability of the chain  $(\theta_l)$  not reaching set  $A$  in  $h$  iterations is

$$\begin{aligned} P(\theta_2 \notin A, \dots, \theta_h \notin A) &= \int_{A^c} \cdots \int_{A^c} K(\theta_1, \theta_2) \cdots K(\theta_{h-1}, \theta_h) d\theta_h \cdots d\theta_2 \\ &= \underbrace{\int_{A^c} \cdots \int_{A^c} K(\theta_1, \theta_2) \cdots K(\theta_{h-2}, \theta_{h-1})}_{h-2} \left\{ \int_{A^c} K(\theta_{h-1}, \theta_h) d\theta_h \right\} d\theta_{h-1} \cdots d\theta_2 \\ &\leq \underbrace{\int_{A^c} \cdots \int_{A^c} K(\theta_1, \theta_2) \cdots K(\theta_{h-2}, \theta_{h-1})}_{h-2} \underbrace{\left\{ 1 - \inf_{\theta_{h-1}} \int_A K(\theta_{h-1}, \theta_h) d\theta_h \right\}}_{1-\rho} d\theta_{h-1} \cdots d\theta_2 \leq (1-\rho)^{h-1}. \end{aligned}$$

Define the stopping time at  $A$  as  $\tau_A = \inf\{l > 1; \theta_l \in A\}$ , we have that

$$p_{\theta}(\tau_A < \infty) = 1 - \lim_{h \rightarrow \infty} \{p_{\theta}(\tau_A > h)\} = 1$$

for any initial point  $\theta$ . By Proposition 4.4.9 in Robert et al. (1999), we can show that  $P_{\theta}(\eta_A = \infty) = 1$  when  $P_{\theta}(\tau_A < \infty)$  for every  $\theta \in A$ . Therefore,  $A$  is Harris recurrent. With the irreducibility given in Lemma 3.3, we complete the proof.  $\square$

**Lemma 3.6.** [Invariant Finite Measure] *There exists an invariant finite measure  $\pi(\cdot)$  for the chain  $(\theta_l)$ , and, hence,  $(\theta_l)$  is Harris positive.*

*Proof.* By Lemma 3.5,  $(\theta_l) = (\tilde{\mathbf{F}}_l, \gamma_l, \Sigma_l)$  is a recurrent chain, and, therefore,  $(\tilde{\mathbf{F}}_l)$  is also a recurrent chain. By Thm 4.5.4 in Robert et al. (1999), there exists an invariant  $\sigma$ -finite measure  $\pi_{\tilde{\mathbf{F}}}(\cdot)$  (unique up to a multiplicative factor) for chain  $(\tilde{\mathbf{F}}_l)$  on space  $\Omega^g$ . Further, since  $\Omega^g$  is compact, any  $\sigma$ -finite measure on  $\Omega^g$  must be finite. In particular,  $\pi_{\tilde{\mathbf{F}}}(\Omega^g) < \infty$ . Now, for any  $B \in \mathcal{B}(\Theta)$ , given the fact that  $K(\theta, B) = K(\tilde{\mathbf{F}}, B)$ , we can define a measure  $\pi(\cdot)$  on  $\Theta$  through

$$\pi(B) = \int_{\Omega^g} K(\tilde{\mathbf{F}}, B) \pi_{\tilde{\mathbf{F}}}(d\tilde{\mathbf{F}}) \quad (3.4)$$

As shown in Lemma 3.1,  $K(\tilde{\mathbf{F}}, \Theta) = 1$ , and, hence,  $\pi(\Theta) = \int_{\Omega^g} K(\tilde{\mathbf{F}}, \Theta) \pi_{\tilde{\mathbf{F}}}(d\tilde{\mathbf{F}}) = \pi_{\tilde{\mathbf{F}}}(\Omega^g) < \infty$ . Moreover, since  $\pi_{\tilde{\mathbf{F}}}(\cdot)$  is the unique invariant measure for  $(\tilde{\mathbf{F}}_l)$ ,

$$\pi_{\tilde{\mathbf{F}}}(A) = \int_{\Omega^g} K(\tilde{\mathbf{F}}, \{\theta' : \tilde{\mathbf{F}}' \in A\}) \pi_{\tilde{\mathbf{F}}}(d\tilde{\mathbf{F}}) = \pi(\{(\tilde{\mathbf{F}}, \gamma, \Sigma) \in \Theta : \tilde{\mathbf{F}} \in A\}), \quad \forall A \in \mathcal{B}(\Omega^g).$$

Therefore, (3.4) can be written as

$$\pi(B) = \int_{\Theta} K(\theta, B) \pi(d\theta)$$

Hence,  $\pi(\cdot)$  is the invariant finite measure for the chain  $(\theta_l)$ , and, therefore,  $(\theta_l)$  is Harris positive. □

### 3.3. Connection and Difference between ProjMC<sup>2</sup> and BSF model

We have established that the chain generated by ProjMC<sup>2</sup> will converge to a valid target distribution  $\pi(\cdot)$ . Based on the implementation of projection and its connection to the BSF model in the algorithm construction, a natural question arises:

*Is  $\pi(\cdot)$  essentially the original BSF model's posterior with  $\mathbf{F}$  projected onto  $\Omega^g$  via  $g(\cdot)$ ?*

The short answer is no. To understand why, note that ProjMC<sup>2</sup> for the BSF model can be interpreted as a Gibbs sampler. Specifically, the density  $\pi(\gamma, \Sigma \mid \tilde{\mathbf{F}} = \tilde{\mathbf{F}}_0, \mathbf{Y})$  coincides with  $p(\gamma, \Sigma \mid \tilde{\mathbf{F}} = \tilde{\mathbf{F}}_0, \mathbf{Y})$  for the original BSF model. Here,  $p(\cdot)$  denotes the conditional distributions in the original BSF model. Let  $p(\mathbf{F}, \gamma, \Sigma \mid \mathbf{Y})$  be the target posterior of the original BSF model. The direct projection of this posterior onto  $\Theta$  is  $\int_{g^{-1}(\tilde{\mathbf{F}})} p(\mathbf{F}, \gamma, \Sigma \mid \mathbf{Y}) d\mathbf{F}$ . If we conjecture that  $\pi(\tilde{\mathbf{F}}, \gamma, \Sigma \mid \mathbf{Y}) = \int_{g^{-1}(\tilde{\mathbf{F}})} p(\mathbf{F}, \gamma, \Sigma \mid \mathbf{Y}) d\mathbf{F}$ , then one would require

$$\pi(\gamma, \Sigma \mid \tilde{\mathbf{F}}, \mathbf{Y}) \propto \frac{\pi(\tilde{\mathbf{F}} \mid \gamma, \Sigma, \mathbf{Y}) \pi(\gamma, \Sigma \mid \mathbf{Y})}{\pi(\tilde{\mathbf{F}} = \tilde{\mathbf{F}}_0 \mid \gamma, \Sigma, \mathbf{Y}) \pi(\gamma, \Sigma \mid \mathbf{Y})} \times \pi(\gamma, \Sigma \mid \tilde{\mathbf{F}} = \tilde{\mathbf{F}}_0, \mathbf{Y}).$$

A more detailed manipulation shows that this condition implies  $p(\gamma, \Sigma, \mathbf{F} = \tilde{\mathbf{F}}_0 \mid \mathbf{Y}) / \int_{g^{-1}(\tilde{\mathbf{F}}_0)} p(\mathbf{F}, \gamma, \Sigma \mid \mathbf{Y}) d\mathbf{F}$  must be independent of  $\tilde{\mathbf{F}}_0$ . This is nontrivial and typically does not hold, even under simple transformations (e.g., shifting columns of  $\mathbf{F}$ ). In fact, obtaining a closed-form expression for the ProjMC<sup>2</sup> target, even up to a proportionality constant, is itself quite challenging.

**A “Squeezed” Pseudo-Posterior:** Although the ProjMC<sup>2</sup> target differs from a direct projection of the BSF posterior, it acts as a “squeezed” pseudo-posterior that combines the original likelihood with the original priors, but under certain integrative constraints. To see this, observe that the conditional distribution for  $\tilde{\mathbf{F}} \mid \mathbf{Y}, \gamma, \Sigma$  in ProjMC<sup>2</sup> is proportional to

$$\int_{g^{-1}(\tilde{\mathbf{F}})} \underbrace{\text{MN}(\mathbf{Y} \mid \mathbf{X}\beta + \mathbf{F}\Lambda, I_n, \Sigma)}_{\text{likelihood}} \times \underbrace{\prod_{k=1}^K N(\mathbf{f}_k \mid 0, C_k)}_{\text{prior of } \mathbf{F}} d\mathbf{F}.$$

On the other hand, if we condition on  $\tilde{\mathbf{F}}$ , the distribution of  $\gamma, \Sigma \mid \tilde{\mathbf{F}}, \mathbf{Y}$  is proportional to

$$\underbrace{\text{MN}(\mathbf{Y} \mid \mathbf{X}\boldsymbol{\beta} + \tilde{\mathbf{F}}\boldsymbol{\Lambda}, I_n, \Sigma)}_{\text{likelihood}} \times \underbrace{\text{MNIW}(\gamma, \Sigma \mid \boldsymbol{\mu}_\gamma, \mathbf{V}_\gamma, \boldsymbol{\Psi}, \nu)}_{\text{prior of } \gamma, \Sigma},$$

where  $\boldsymbol{\mu}_\gamma = [\boldsymbol{\mu}_\beta^\top : \boldsymbol{\mu}_\Lambda^\top]^\top$ ,  $\mathbf{V}_\gamma = [\mathbf{V}_\beta^\top : \mathbf{V}_\Lambda^\top]^\top$ . Hence, while the ProjMC<sup>2</sup> target is not the same as the original BSF posterior (with a simple projection), the samples are drawn from a distribution that incorporates both the likelihood and the original priors—albeit modified or “squeezed”. This modification stems from the way  $\tilde{\mathbf{F}}$  is integrated over or restricted to the manifold defined by  $g(\cdot)$ , rather than being drawn directly from the support of  $\mathbf{F}$ .

## 4. SCALABLE BSF MODELS AND SAMPLING ALGORITHMS

### 4.1. Scalable Modeling

This subsection addresses scalable extensions of the Bayesian Spatial Factor (BSF) model and its efficient implementation through the ProjMC<sup>2</sup> sampling algorithm.

**Sampling of  $\mathbf{F}$ :** The primary computational challenge in the proposed algorithm lies in efficiently sampling the high-dimensional  $n \times K$  factor matrix  $\mathbf{F}$ . To achieve computational scalability with respect to the number of spatial locations (spots)  $n$ , a Nearest-Neighbor Gaussian Process (NNGP) (Datta et al., 2016) is employed. NNGP provides a sparse, full-rank approximation of a full Gaussian process, effectively capturing localized and global spatial dependence while ensuring linear computational and storage complexity in  $n$ . Specifically, each latent factor  $f_k(\mathbf{s})$  for  $\mathbf{s} \in \mathcal{D}$  is endowed with an NNGP prior,  $\text{NNGP}(0, \rho_{\psi_k}(\cdot, \cdot))$ , implying that  $\mathbf{f}_k \sim \mathcal{N}(\mathbf{0}, \boldsymbol{\rho}_k)$ , where  $\boldsymbol{\rho}_k = (\mathbf{I} - \mathbf{A}_{\rho_k})^{-1} \mathbf{D}_{\rho_k} (\mathbf{I} - \mathbf{A}_{\rho_k})^{-\top}$ . Here, the matrices  $\mathbf{A}_{\rho_k}$  (sparse, lower-triangular) and  $\mathbf{D}_{\rho_k}$  (diagonal) are constructed based on conditional expectations and variances derived from the Gaussian process covariance function  $\rho_{\psi_k}(\mathbf{s}, \mathbf{s}')$ . The parameter  $m$ , representing the number of neighbors in the NNGP, is typically set below 20 for computational efficiency.

Consider a predetermined ordering of spatial locations  $\mathcal{S} = s_1, \dots, s_n$ . For each location  $\mathbf{s}_i$ , define  $N_m(\mathbf{s}_i)$  as the set containing up to  $m$  nearest neighbors among locations  $\mathbf{s}_j \in \mathcal{S}$  with index of order  $j < i$ . The  $(i, j)$ -th entry of  $\mathbf{A}_{\rho_k}$  is 0 whenever  $\mathbf{s}_j \notin N_m(\mathbf{s}_i)$ . If  $j_1 < j_2 < \dots < j_m$  are the  $m$  column indices for the nonzero entries in the  $i$ -th row of  $\mathbf{A}_{\rho_k}$ , then the  $(i, j_k)$ -th element of  $\mathbf{A}_{\rho_k}$  is the  $k$ -th element of the  $1 \times m$  vector  $\mathbf{a}_i^\top = \boldsymbol{\rho}_{\psi_k}(\mathbf{s}_i, N_m(\mathbf{s}_i)) \boldsymbol{\rho}_{\psi_k}(N_m(\mathbf{s}_i), N_m(\mathbf{s}_i))^{-1}$ . The  $(i, i)$ -th diagonal element of  $\mathbf{D}_{\rho_k}$  is given by  $\rho_{\psi_k}(\mathbf{s}_i, \mathbf{s}_i) - \mathbf{a}_i^\top \boldsymbol{\rho}_{\psi_k}(N_m(\mathbf{s}_i), \mathbf{s}_i)$ . Repeating these calculations for each row completes the construction of  $\mathbf{A}_{\rho_k}$  and  $\mathbf{D}_{\rho_k}$ .



For ordering the locations, the maximin ordering has been shown to be robust and efficient for Vecchia approximations (Katzfuss and Guinness, 2021; Guinness, 2018). For implementation, the maximin ordering can be computed in quasilinear time in  $n$  (Schäfer et al., 2021). Following the construction of ProjMC<sup>2</sup> in the preceding section, we prefix  $\Psi_k$ , which allows us to expedite MCMC sampling by precomputing the matrices  $\mathbf{D}_{\rho_k}$  and  $\mathbf{A}_{\rho_k}$ . This step, amenable to parallelization, has complexity  $\mathcal{O}(n \cdot m^3 \cdot K) = \mathcal{O}(n)$  when  $m \ll n$ .

By modeling  $f_k(\mathbf{s})$  using NNGP, the cost of a direct sample of  $\mathbf{F}$  from the high-dimensional Gaussian distribution (2.6) can be reduced from  $\mathcal{O}(n^3)$  to  $\mathcal{O}(n)$ . Recall that the  $\mathbf{L}_k^{-1}$  in  $\tilde{\mathbf{X}}$  is now  $\mathbf{L}_k^{-1} = \mathbf{D}_{\rho_k}^{-1/2}(\mathbf{I} - \mathbf{A}_{\rho_k})$ , which implies that the number of nonzero elements in  $\tilde{\mathbf{X}}$  grows linearly with  $n$ . Such inherent sparsity facilitates efficient conjugate gradient algorithms (Zhang et al., 2019; Nishimura and Suchard, 2023; Zhang, 2022). More concretely, obtaining a sample from (2.6) reduces to solving the linear system  $\tilde{\mathbf{X}}\mathbf{x} = (\tilde{\mathbf{Y}} + \mathbf{v})$ , where the elements of  $\mathbf{v}$  are drawn independently from a standard normal distribution. In our implementation, we employ the iterative LSMR method, a robust solver for sparse linear systems that avoids explicitly forming the matrix  $\tilde{\mathbf{X}}^\top \tilde{\mathbf{X}}$  (Fong and Saunders, 2011). When generating  $\tilde{\mathbf{F}} = g(\mathbf{F})$ , we employ the modified Gram-Schmidt to perform a thin QR decomposition. This approach is particularly efficient when  $n \gg K$ , with total cost in  $\mathcal{O}(nK^2)$  (Golub and Van Loan, 2012). Detailed algorithmic procedures are provided in Supplement S.1. Finally, while the discussion focuses on the NNGP approach, some of the computational strategies presented for sampling  $\mathbf{F}$  can be adapted or modified for use with other scalable spatial modeling approach. See Zhang and Banerjee (2022) for related discussions.

**Modeling of  $\Sigma$ :** When considering an application for spatial transcriptomic data, the number of outcomes (genes)  $q$  typically ranges from hundreds to tens of thousands. To ensure computational scalability, it is assumed that the dominant correlation structure is captured by predictors ( $\mathbf{X}\beta$ ) and low-dimensional embeddings ( $\mathbf{F}\Lambda$ ), and a diagonal structure is adopted for the covariance matrix  $\Sigma$ . Specifically, let  $\Sigma = \bigoplus_{i=1}^q \{\sigma_i^2\}$  with  $\sigma_i^2 \sim \text{IG}(a, b_i)$  prior, the conditional posterior for each  $\sigma_i^2$  in the BSF model remains inverse-gamma

$$\sigma_i^2 \mid (\mathbf{Y}, \mathbf{F}) \sim \text{IG}(a^*, b_i^*), \quad (4.1)$$

where  $a^* = a + \frac{n}{2}$ ,  $b_i^* = b_i + \frac{1}{2}(\mathbf{Y}^* - \mathbf{X}^*\boldsymbol{\mu}^*)_i^\top (\mathbf{Y}^* - \mathbf{X}^*\boldsymbol{\mu}^*)_i$ . Here  $(\mathbf{Y}^* - \mathbf{X}^*\boldsymbol{\mu}^*)_i$  denotes the  $i$ -th column of  $\mathbf{Y}^* - \mathbf{X}^*\boldsymbol{\mu}^*$ . From (2.5),  $\gamma \mid \Sigma, \mathbf{F}, \mathbf{Y} \sim \text{MN}(\boldsymbol{\mu}^*, \mathbf{V}^*, \Sigma)$ .

**Initialization:** To facilitate efficient convergence of the MCMC algorithm, the regression parameters  $\beta$  are initialized using ordinary least squares estimation  $(\mathbf{X}^\top \mathbf{X})^{-1} \mathbf{X}^\top \mathbf{Y}$ . The latent factor matrix  $\mathbf{F}$  and the loading matrix  $\Lambda$  are initialized via principal component analysis (PCA) applied to residuals obtained from the initial regression fit,  $\mathbf{Y} - \mathbf{X}\beta$ . Considering that PCA is employed solely for initialization and will

subsequently be updated through MCMC iterations—and given the potentially large dimensions of  $n$  and  $q$ —randomized SVD is adopted to ensure computational complexity scales linearly with respect to  $n$  and  $q$  Halko et al. (2011); Martinsson and Tropp (2020). It is recommended to arrange the latent factor and loading matrices such that the factors are ordered by decreasing empirical spatial range (i.e., decreasing smoothness), enhancing convergence stability as discussed in detail in the following subsection. Finally, diagonal entries of  $\Sigma$  can be initialized using residual variances from the initial regression fit,  $\mathbf{Y} - \mathbf{X}\beta$ . A simplified algorithmic summary is presented in equation (1), with comprehensive details available in Supplement S.1.

---

**Algorithm 1** ProjMC<sup>2</sup> for NNGP based BSF model with diagonal  $\Sigma$

---

- 1: **Input:** Design matrix  $\mathbf{X}$ , outcomes  $\mathbf{Y}$ , set of spots  $\chi$ , prior parameters, prefixed parameters, and number of MCMC iterations  $L$ .
  - 2: **Preallocation, precomputation, and initialization**  
*(Includes preallocation of necessary matrices, construction of the maximin ordering of  $\chi$ , precomputation of matrices  $\mathbf{D}_{\rho_k}$  and  $\mathbf{A}_{\rho_k}$ , and initialization of parameters for MCMC.)*
  - 3: **for**  $l = 1, \dots, L$  **do**
  - 4:   Sample  $\mathbf{F}^{(l)}$  by solving linear system  $\tilde{\mathbf{X}}x = (\tilde{\mathbf{Y}} + v)$ , with  $v \sim N(0, \mathbf{I})$ , using LSMR.
  - 5:   Generate projected embeddings  $\tilde{\mathbf{F}}^{(l)} = g(\mathbf{F}^{(l)})$ . *(Update  $\mathbf{X}^*$  in (2.5) by replacing  $\mathbf{F}$  with  $\tilde{\mathbf{F}}^{(l)}$ .)*
  - 6:   Sample covariance matrix  $\Sigma^{(l)}$  using (4.1).
  - 7:   Sample parameters  $(\beta^{(l)}, \Lambda^{(l)})$  from  $\text{MN}(\mu^*, \mathbf{V}^*, \Sigma^{(l)})$ .
  - 8: **end for**
  - 9: **Output:** Posterior samples  $\{\tilde{\mathbf{F}}^{(l)}, \beta^{(l)}, \Lambda^{(l)}\}_{l=1, \dots, L}$  of low-dimensional embeddings, regression coefficients, and loading matrix.  
*(Retain posterior samples after the warm-up period; thinning, i.e., keeping one iteration per several iterations, can be used to reduce storage.)*
- 

## 4.2. Implementation and Practical Considerations

**Convergence and Mixing in Practice:** While theoretical results guarantee that ProjMC<sup>2</sup> for the BSF model converges to its stationary distribution regardless of initialization, posterior multimodality remains possible despite restricting factor matrix samples to the space  $\Omega^g$ . This concern arises naturally because  $\Omega^g$  is closed under permutations and sign changes of factors. Such inherent symmetry induces identifiability issues within the likelihood function, complicating the posterior landscape and potentially leading to slower MCMC mixing and more complex convergence rate analyses.

Empirically, however, ProjMC<sup>2</sup> demonstrates greater stability than initially anticipated. Simulation studies consistently indicate that recovered factors tend to organize themselves by decreasing smoothness. Columns of the projected factor matrix  $\tilde{\mathbf{F}}$  naturally order themselves, placing smoother factors in initial columns and noisier factors in subsequent columns. The empirical investigation attributes this observed stability primarily to the QR decomposition step within the projection  $g(\cdot)$ .

To intuitively illustrate this phenomenon, consider a simplified scenario with two factors, and we represent the factor matrix prior to projection as  $\mathbf{F} = [\mathbf{f}_1, \mathbf{f}_2]$ . Suppose that  $\mathbf{f}_1 \sim \mathcal{N}(\mu_1, C_1)$  and  $\mathbf{f}_2 \sim \mathcal{N}(\mu_2, C_2)$ . The projected factor matrix via QR decomposition,  $\tilde{\mathbf{F}} = [\tilde{\mathbf{f}}_1, \tilde{\mathbf{f}}_2]$ , is given by  $\tilde{\mathbf{f}}_1 = \mathbf{f}_1 / \|\mathbf{f}_1\|$ , followed by  $\tilde{\mathbf{f}}_2 = \mathbf{f}_2 - (\tilde{\mathbf{f}}_1^\top \mathbf{f}_2) \tilde{\mathbf{f}}_1$  and normalization  $\tilde{\mathbf{f}}_2 = \tilde{\mathbf{f}}_2 / \|\tilde{\mathbf{f}}_2\|$ . When the initial factor  $\mathbf{f}_1$  exhibits strong correlations (smoothness), QR projection introduces minimal perturbations in subsequent factors. Consequently, posterior distributions concentrate in regions of  $\Omega^8$  favoring this smooth-to-noisy factor ordering. Conversely, placing less correlated (noisy) factors first increases perturbations, dispersing posterior mass and reducing local density.

Hence, the QR projection implicitly induces a preferred ordering of factor embeddings based on the underlying correlation structure, thereby enhancing sampling stability. Although it remains theoretically challenging to fully capture all posterior modes using finite-length MCMC chains, the empirical findings suggest that the QR-induced ordering substantially enhances practical stability and sampling efficiency.

**Postprocessing for Label Switching Issue:** Although the QR decomposition can enhance identifiability, it does not resolve the so-called label-switching issues inherent in the proposed BSF models. In practice, MCMC samples for rows of the loading matrix  $\mathbf{\Lambda}$  often oscillate between two symmetric modes, where the signs of all elements within a row simultaneously switch. Direct posterior summarization of these draws without correcting for label switching can lead to misleading inference (Stephens, 2000). To mitigate this issue, we employ a post-processing approach to align samples from the minor mode with the dominant mode (Stephens, 2000; Gelman et al., 2013, Section 22.3). Specifically, the posterior mean of each row of the loading matrix is first computed from the MCMC chains after warm-up. Then, at each iteration, check the sign of its inner product with the current draw. If negative, flip the signs of the row and corresponding latent factor. This realignment ensures coherent posterior summaries.

## 5. SIMULATION

The response  $\mathbf{y}(\mathbf{s})$  was simulated from the spatial factor model in (2.1) with  $q = 10$ ,  $p = 2$ ,  $K = 2$ , and a diagonal  $\mathbf{\Sigma}$  over  $n = 2000$  randomly generated locations over a unit square. The explanatory variable  $\mathbf{x}(\mathbf{s})$  consists of an intercept and a single predictor generated from a standard normal. Each  $f_k(\mathbf{s})$  was generated using an exponential covariance function, i.e.,  $\rho_{\psi_k}(\mathbf{s}, \mathbf{s}') = \exp(-\phi_k \|\mathbf{s} - \mathbf{s}'\|)$ , for  $\mathbf{s}, \mathbf{s}' \in \mathcal{D}$ , where  $\|\mathbf{s} - \mathbf{s}'\|$  is the Euclidean distance between  $\mathbf{s}$  and  $\mathbf{s}'$ , and  $\psi_k = \phi_k$  is the decay for each  $k$ . The true decay parameters used to generate  $f_1(\mathbf{s})$  and  $f_2(\mathbf{s})$  were 6.0 and 9.0, respectively. In the specified priors, the decay parameters for  $f_1(\mathbf{s})$  and  $f_2(\mathbf{s})$  were intentionally set at 4.0 and 6.0, respectively, to simulate a scenario where the decay rates are misspecified or underestimated, which is a common occurrence in

---

practice. The exact values for the remaining parameters are provided in Supplement S.2. A flat prior was assigned for  $\beta$  and  $\Lambda$  and  $\text{IG}(2, 1.0)$  priors were assigned for the diagonal elements of  $\Sigma$ . The priors for the latent spatial factors are modeled through NNGP with the number of neighbors  $m = 15$ . This simulation study evaluates both the block update MCMC sampling algorithm (Gibbs) and the proposed ProjMC<sup>2</sup> algorithm. The posterior inference for each model was based on MCMC chains with 15,000 iterations after a burn-in of 5,000 iterations. All models were run on an Apple MacBook Pro with an M2 Max chip, 12-core CPU (8 performance and 4 efficiency cores), and 96 GB of unified memory, running macOS 14.6.1 (Sonoma). Convergence diagnostics and other posterior summaries were implemented within the Julia statistical environment.

## 5.1. Simulation Results

**Convergence and Mixing Rate Evaluation:** This study first investigates the impact of the proposed MCMC algorithm on convergence and mixing rate by comparing three different MCMC approaches. The baseline approach is the standard blocked Gibbs sampler. As previously discussed, certain non-identifiability issues can be mitigated through appropriate post-processing techniques. Among several post-processing methods tested, it was found that recentering spatial factors at zero yielded the most substantial improvement in convergence and mixing rate. Therefore, the second approach examined is the blocked Gibbs sampler augmented with post-processing. The third method is the proposed ProjMC<sup>2</sup> algorithm.

Table 1 summarizes the effective sample sizes (ESS) for all model parameters across these three methods. Figure 2 presents trace plots for weakly-identifiable parameters, including intercepts ( $\beta_0$ , the first row of  $\beta$ ) and loadings (elements of  $\Lambda$ ). From Table 1, it is evident that identifiable parameters, i.e., the regression coefficients ( $\beta_1$ , the second row of  $\beta$ ) and the noise covariance matrix  $\Sigma$ , are consistently well-estimated by all approaches, each producing minimum ESS values greater than 5,000.

For the intercepts ( $\beta_0$ ), substantial improvements in convergence and mixing are achieved through recentering latent spatial factors, whether via post-processing or ProjMC<sup>2</sup>. Post-processing modestly improves the mixing rate of certain spatial factor components ( $F$ ), elevating the minimum and median ESS from 41 and 68 to 44 and 245, respectively, across  $2 \times 2,000$  parameters. Nevertheless, for parameters involving the loading matrix ( $\Lambda$ ) and latent spatial factors ( $F$ ), stable and efficient MCMC chains were only obtained through the ProjMC<sup>2</sup> method. Specifically, ProjMC<sup>2</sup> significantly increased the minimum and median ESS for spatial factors from 44 and 245 to 551 and 12,298, respectively. And all loading matrix elements, initially with ESS values below 50 under the first two methods, attained ESS values exceeding 100. Moreover, trace plots in Figure 2 demonstrate rapid convergence of all MCMC chains produced

	Gibbs		Gibbs + Post		ProjMC <sup>2</sup>	
ESS	(min/mean/med)	<100	(min/mean/med)	<100	(min/mean/med)	<100
$\beta_0$	38/41/42	100%	7300/11764/12302	0%	8635/12331/12787	0%
$\beta_1$	6616/11201/11882	0%	6616/11201/11882	0%	7991/11938/12480	0%
$\Lambda$	36/44/41	100%	36/42/39	100%	199/2644/386	0%
$F$	41/67/68	100%	44/2187/245	23%	551/10275/12298	0%
$\Sigma$	5392/10516/12225	0%	5392/10516/12225	0%	7601/11529/12746	0%

Table 1: Comparison of effective sample size (ESS)—reported as minimum, mean, and median, and the proportion of variables with low ESS values (ESS < 100)— across three methods: the original blocked Gibbs sampler (Gibbs), Gibbs with post-processing (Gibbs + Post), and the proposed Projected MCMC (ProjMC<sup>2</sup>). Results are shown for the intercepts  $\beta_0$ , regression coefficients  $\beta_1$ , loading matrix  $\Lambda$ , matrix of latent factors  $F$ , and the noise covariance matrix  $\Sigma$ , based on MCMC chains of 20,000 iterations with the first 5,000 iterations discarded as warm-up.

by ProjMC<sup>2</sup>, reaching high-probability regions within a relatively small number of iterations. Although loading parameters exhibit relatively slower mixing, convergence occurs reliably within a few hundred iterations, underscoring the effectiveness of the proposed approach.

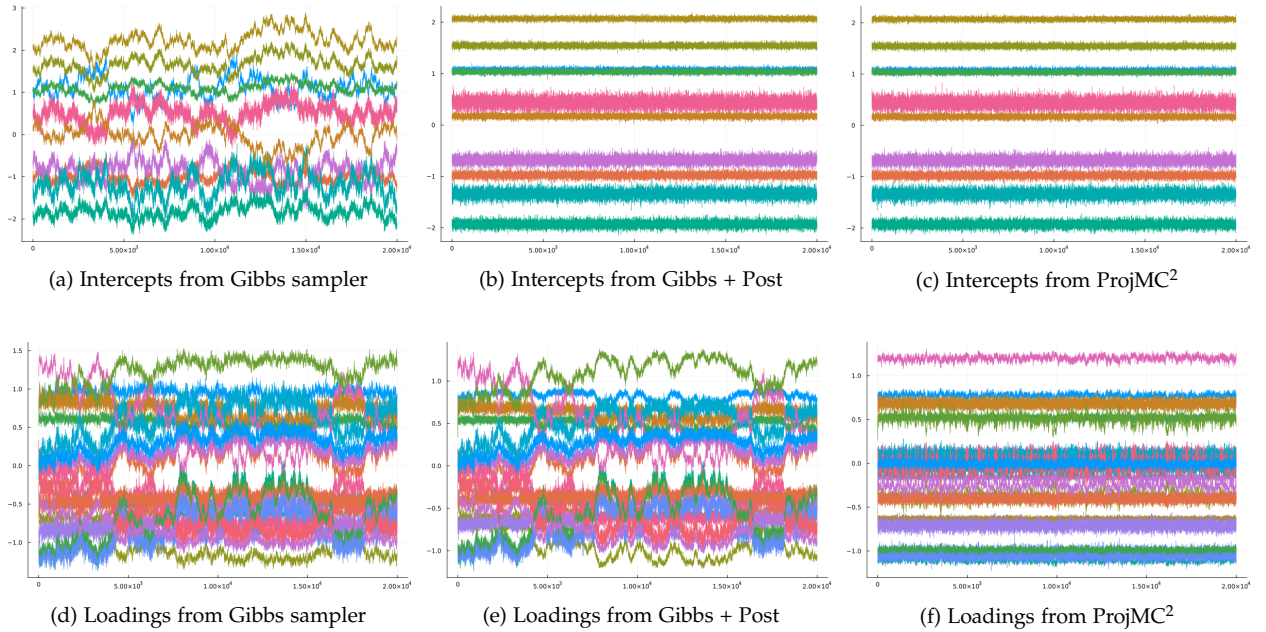


Figure 2: Trace plots of MCMC chains for weakly identifiable parameters: the intercepts (top row) and loading matrix  $\Lambda$  (bottom row). Columns correspond to results from the blocked Gibbs sampler (left), Gibbs sampler with post-processing (middle), and ProjMC<sup>2</sup> (right).

**Inference Accuracy** **Inference Accuracy:** Following the convergence and mixing rate study, we now evaluate how accurately each sampler recovers the underlying spatial-factor patterns. Guided by the previous findings, this evaluation focuses on the post-processed blocked Gibbs sampler (hereafter, Gibbs+Post) and

---

the proposed ProjMC<sup>2</sup> algorithm. To compare the inference accuracy of the high-dimensional spatial factors across different algorithms, both the true factor and all posterior samples were projected on to the unit sphere  $\mathcal{S}^{n-1}$ . Recognizing that ProjMC<sup>2</sup> operates by constraining the posterior samples of factors to the Stiefel manifold, an additional projection of the true latent factors onto this manifold was performed for the ProjMC<sup>2</sup> outputs' evaluation. For each factor, the point estimate is derived using the Fréchet mean (or mean direction) of its posterior samples Mardia and Jupp (2009).

Figure 3 provides a visual comparison between the projected true latent spatial factors and their point estimates obtained from each method. It is pertinent to recall that the selection of decay parameters, intentionally chosen to be larger than their true values, predisposes the recovered factors towards smoother spatial patterns than the truth. A sensitivity analysis examining the impact of less restrictive priors is presented in Section 5.2. Visual inspection of Figure 3 indicates that both Gibbs+Post and ProjMC<sup>2</sup> successfully capture the dominant spatial patterns present in both factors ( $\mathbf{f}_1$  and  $\mathbf{f}_2$ ). However, a closer examination reveals differences in the recovery of more subtle features. The factors estimated via ProjMC<sup>2</sup> appear to accentuate patterns that are distinct to each factor. Conversely, Gibbs+Post sometimes yields estimates where subtle patterns exhibit similarity across different factors. This tendency in ProjMC<sup>2</sup> is likely attributable to the inherent constraints imposed by sampling on the Stiefel manifold, which enforces stricter orthogonality.

Quantitative assessment of inference accuracy is based on two metrics, summarized in Table 2. First, the fidelity of the point estimate is measured by the Euclidean distance between the estimated Fréchet mean and the appropriately projected true factor. Second, the concentration or stability of the posterior distribution for each factor is quantified by the spherical variance, calculated as  $1 - \bar{R}^2$ , where  $\bar{R}$  is the Euclidean norm of the sample mean vector, computed using the posterior samples projected onto the unit sphere. Numerically, the performance of the two algorithms appears comparable, as shown in Table 2. Overall, ProjMC<sup>2</sup> yields slightly more accurate point estimates, indicated by marginally lower Euclidean distances. It is crucial to acknowledge, however, that this comparison is not entirely direct, as the target “true” values differ due to the distinct projection methods (centering and scaling for Gibbs+Post vs. Stiefel manifold projection for ProjMC<sup>2</sup>). Furthermore, the resulting posterior distributions approximated by the two methods inherently differ. The observed accuracy and variance metrics reflect a complex interplay between the flexibility of the posterior representation, the algorithm’s convergence behavior, and its mixing efficiency during posterior sampling.

Finally, the posterior inference for the identifiable model parameters were assessed, specifically the regression coefficient matrix  $\boldsymbol{\beta}$  (encompassing intercepts  $\boldsymbol{\beta}_0$  and slope coefficients  $\boldsymbol{\beta}_1$ ) and the diagonal elements of the noise covariance matrix  $\boldsymbol{\Sigma}$ . Detailed posterior summaries, including posterior means

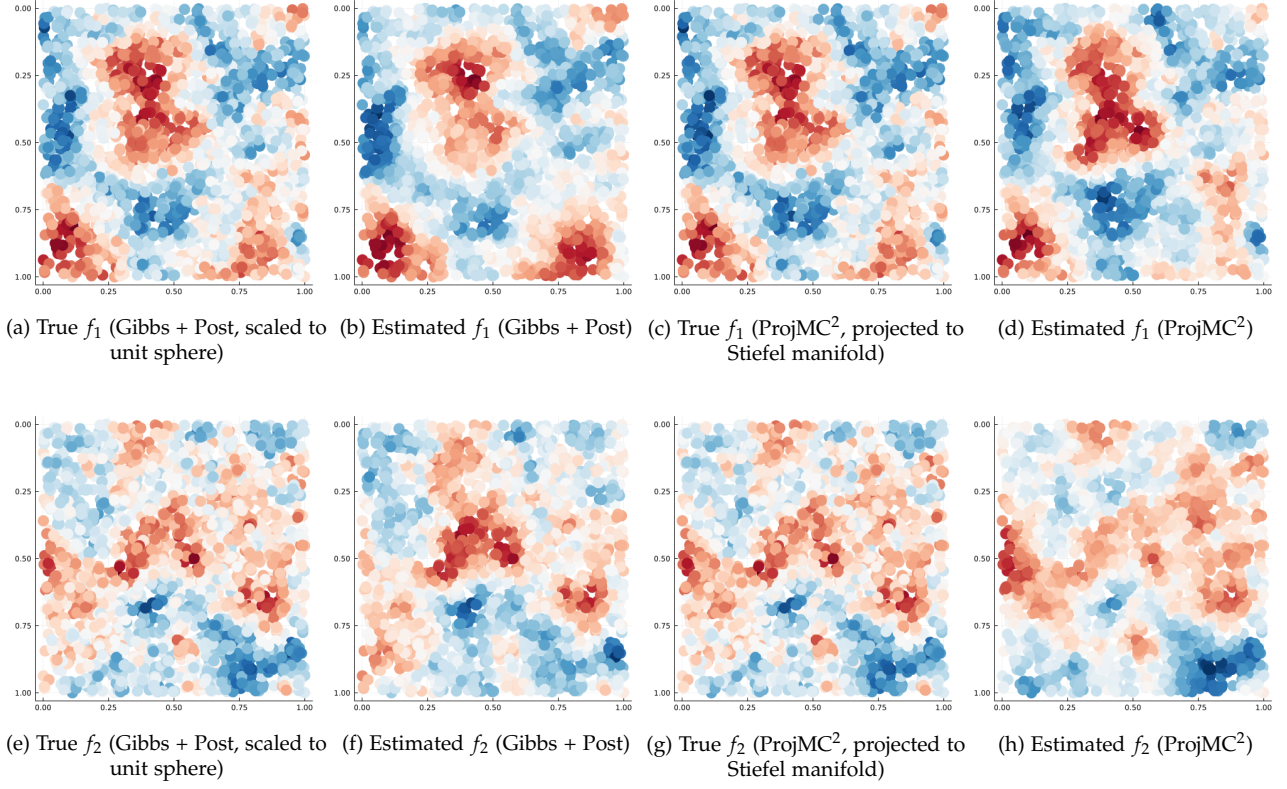


Figure 3: Scatter plots comparing the true and estimated posterior mean of the two latent spatial factors,  $f_1$  (top row) and  $f_2$  (bottom row). Dot locations indicate spatial positions, and colors represent latent factor values. The left two columns show results from the Gibbs sampler with post-processing, and the right two columns show results from the proposed ProjMC<sup>2</sup> method. For Gibbs + Post-processing, the true factors are centered and rescaled to the unit sphere. For ProjMC<sup>2</sup>, the true factors are additionally projected onto the Stiefel manifold. Each pair of true and estimated factors shares the same color scale for visual comparison.

and 95% credible intervals obtained from both the Gibbs+Post sampler and the ProjMC<sup>2</sup> algorithm, are presented alongside the true parameter values in Table 3. Examination of Table 3 reveals that the posterior inference for the regression coefficients  $\beta$  is almost indistinguishable between the two methods. Both approaches yield posterior means that closely approximate the true values, and the corresponding 95% credible intervals demonstrate comparable width and coverage. For the noise variance parameters (diagonal elements of  $\Sigma$ ), the estimates derived from both algorithms are similarly accurate and closely aligned with the true values. Nonetheless, a consistent pattern emerges where ProjMC<sup>2</sup> produces marginally higher posterior mean estimates for these variances compared to the Gibbs+Post sampler. This slight discrepancy may be attributable to the more constrained sampling space imposed in ProjMC<sup>2</sup>; limiting the variation captured by the latent factors might necessitate attributing a slightly larger proportion of the residual variance to the noise term  $\Sigma$ . In summary, both algorithms demonstrate robust and highly comparable performance in estimating the identifiable parameters of the model.

Latent Factor	Gibbs + Post		ProjMC <sup>2</sup>	
	Euclidean Dist.	Sphere Var.	Euclidean Dist.	Sphere Var.
$f_1$	0.408	0.1278	0.405	0.0453
$f_2$	0.5394	0.1237	0.5033	0.1411

Table 2: Comparison of posterior summaries for the two latent spatial factors ( $\mathbf{f}_1$  and  $\mathbf{f}_2$ ) across two methods: Gibbs sampler with post-processing (Gibbs + Post) and the proposed Projected MCMC (ProjMC<sup>2</sup>). Each method is evaluated using two diagnostics: Euclidean distance between the true and estimated factor, and the spherical variance of the posterior samples.

	Gibbs + Post			ProjMC <sup>2</sup>			Gibbs + Post			ProjMC <sup>2</sup>	
	mean	95%CI		mean	95%CI		mean	95%CI		mean	95%CI
$\beta_{[1,1]}$	1.0	1.06	(1.0, 1.13)	1.06	(1.0, 1.13)	$\beta_{[1,6]}$	-1.5	-1.34	(-1.48, -1.2)	-1.34	(-1.48, -1.2)
$\beta_{[1,2]}$	-1.0	-0.97	(-1.06, -0.89)	-0.97	(-1.06, -0.89)	$\beta_{[1,7]}$	0.5	0.44	(0.27, 0.6)	0.44	(0.27, 0.61)
$\beta_{[1,3]}$	1.0	1.04	(0.98, 1.1)	1.04	(0.98, 1.09)	$\beta_{[1,8]}$	0.3	0.17	(0.1, 0.24)	0.17	(0.1, 0.24)
$\beta_{[1,4]}$	-0.5	-0.68	(-0.81, -0.55)	-0.68	(-0.81, -0.55)	$\beta_{[1,9]}$	-2.0	-1.93	(-2.04, -1.82)	-1.93	(-2.04, -1.82)
$\beta_{[1,5]}$	2.0	2.07	(2.01, 2.12)	2.07	(2.01, 2.12)	$\beta_{[1,10]}$	1.5	1.54	(1.48, 1.61)	1.55	(1.48, 1.61)
$\beta_{[2,1]}$	-3.0	-2.9	(-3.02, -2.78)	-2.9	(-3.02, -2.78)	$\beta_{[2,6]}$	3.0	3.05	(2.8, 3.31)	3.05	(2.8, 3.3)
$\beta_{[2,2]}$	2.0	2.02	(1.86, 2.17)	2.02	(1.86, 2.17)	$\beta_{[2,7]}$	4.0	4.01	(3.71, 4.3)	4.0	(3.71, 4.29)
$\beta_{[2,3]}$	2.0	2.01	(1.91, 2.11)	2.01	(1.91, 2.11)	$\beta_{[2,8]}$	-2.5	-2.49	(-2.62, -2.37)	-2.49	(-2.61, -2.37)
$\beta_{[2,4]}$	-1.0	-1.02	(-1.24, -0.8)	-1.02	(-1.25, -0.79)	$\beta_{[2,9]}$	5.0	5.07	(4.88, 5.26)	5.07	(4.87, 5.26)
$\beta_{[2,5]}$	-4.0	-3.98	(-4.08, -3.88)	-3.98	(-4.08, -3.88)	$\beta_{[2,10]}$	-3.0	-2.98	(-3.1, -2.87)	-2.98	(-3.1, -2.87)
$\Sigma_{[1,1]}$	0.5	0.51	(0.48, 0.55)	0.52	(0.49, 0.56)	$\Sigma_{[6,6]}$	2.5	2.61	(2.45, 2.78)	2.62	(2.46, 2.8)
$\Sigma_{[2,2]}$	1.0	1.01	(0.95, 1.08)	1.02	(0.95, 1.08)	$\Sigma_{[7,7]}$	3.5	3.57	(3.35, 3.8)	3.57	(3.36, 3.8)
$\Sigma_{[3,3]}$	0.4	0.41	(0.39, 0.44)	0.41	(0.39, 0.44)	$\Sigma_{[8,8]}$	0.45	0.46	(0.43, 0.5)	0.49	(0.45, 0.52)
$\Sigma_{[4,4]}$	2.0	2.12	(1.99, 2.26)	2.13	(2.0, 2.27)	$\Sigma_{[9,9]}$	1.5	1.57	(1.47, 1.67)	1.58	(1.48, 1.68)
$\Sigma_{[5,5]}$	0.3	0.31	(0.29, 0.34)	0.33	(0.31, 0.35)	$\Sigma_{[10,10]}$	0.5	0.5	(0.47, 0.54)	0.51	(0.48, 0.55)

Table 3: Posterior inference for identifiable model parameters. Comparison of posterior means and 95% credible intervals for regression coefficients ( $\beta$ ) and noise variances (diagonal elements of  $\Sigma$ ) obtained using the Gibbs sampler with post-processing (Gibbs+Post) and the proposed ProjMC<sup>2</sup> algorithm, referenced against the true parameter values.

## 5.2. Sensitivity Analysis

Initial explorations revealed that ProjMC<sup>2</sup> consistently orders estimated spatial factors by decreasing smoothness. This ordering appears driven by the algorithm’s QR decomposition, as it vanishes when this step is excluded. To systematically assess the algorithm’s sensitivity to initial conditions and prior spatial decay parameters ( $\phi_k$ ), and to further clarify the QR decomposition’s role in this smoothness-based ordering, additional simulation experiments were conducted. These experiments employed initial values designed to challenge the algorithm’s inherent ordering. Specifically, regression coefficients ( $\beta$ ) and noise variances (diagonal of  $\Sigma$ ) were initialized at their true values. However, the loading matrix  $\Lambda$  was initialized using its true value but with its two rows permuted, encouraging an initial factor ordering contrary to



the expected smoothness hierarchy ( $f_1$  smoother than  $f_2$ ). Furthermore, we varied the prior spatial decay parameters ( $\phi_1, \phi_2$ ) across three scenarios: 1) **Test 1**:  $\phi_1 = 6.0, \phi_2 = 9.0$ . These values match those used in the data generation process, reflecting moderate prior smoothness beliefs consistent with the true factors. 2) **Test 2**:  $\phi_1 = 9.0, \phi_2 = 3.0$ . This setting imposes stronger prior smoothness on the second factor relative to the first, contradicting the true smoothness relationship. 3) **Test 3**:  $\phi_1 = 18.0, \phi_2 = 18.0$ . These larger decay values correspond to weaker, identical smoothness priors for both factors, representing a less informative scenario.

Visual inspection of the estimated factors (Figure 4) confirms the robustness of the algorithm’s ordering. Across all scenarios, ProjMC<sup>2</sup> consistently recovered factors by decreasing smoothness ( $f_1$  smoother than  $f_2$ ), overriding permuted initializations of  $\Lambda$  and the misaligned priors in Test 2. This strongly indicates the QR decomposition’s dominance in enforcing smoothness-based ordering.

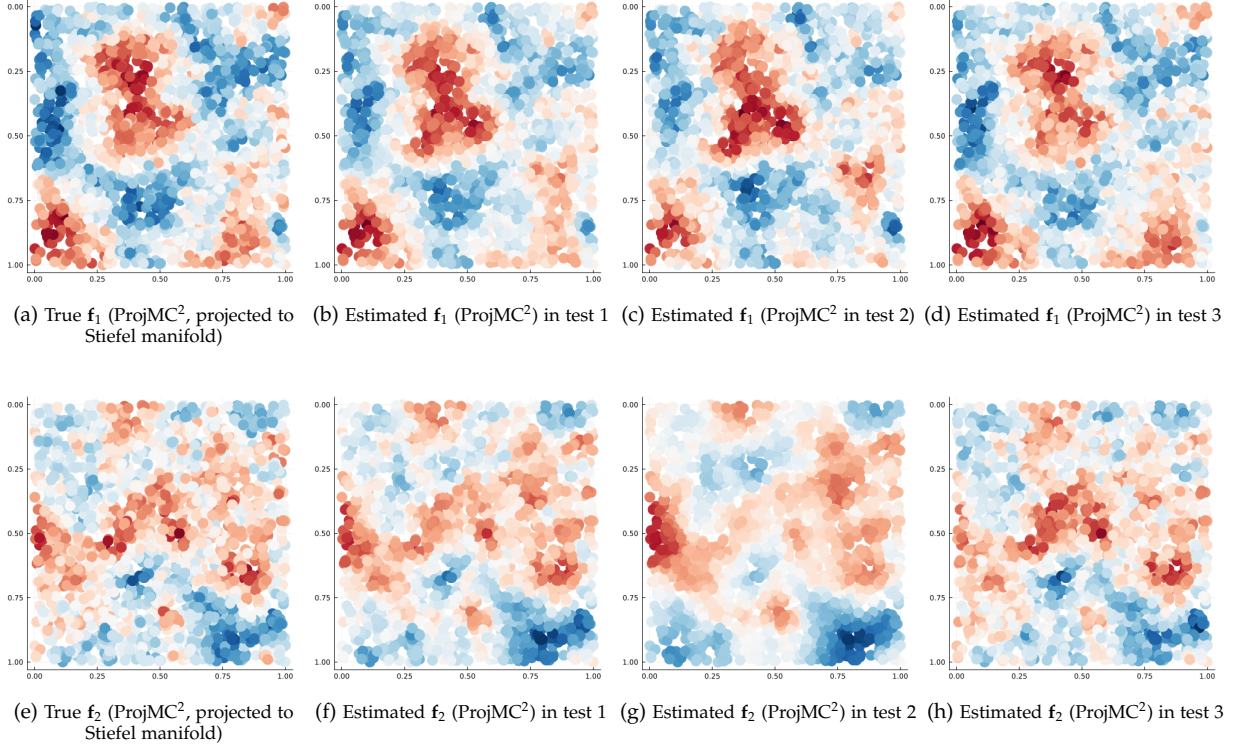


Figure 4: Scatter plots comparing the true and estimated posterior mean of the two latent spatial factors,  $f_1$  (top row) and  $f_2$  (bottom row). Dot locations indicate spatial positions, and colors represent latent factor values. The first column shows the true factors projected onto the Stiefel manifold. The second to fourth columns show the estimated factors for three sensitive tests.

Quantitative MCMC efficiency (ESS) and latent factors inference accuracy (Euclidean distance to true factors, Spherical Variance of posterior samples) are summarized in Table 4 and 5, respectively. Analysis of these metrics highlights an anticipated trade-off mediated by the prior specifications. Stronger or more

informative smoothness priors (Tests 1 and 2) generally lead to more concentrated posterior distributions, as evidenced by higher minimum and median ESS values (Table 4) and lower spherical variances (Table 5) for the challenging parameters in  $\Lambda$  and  $F$ .

ESS	Test 1		Test 2		Test 3	
	(min/mean/med)	<100	(min/mean/med)	<100	(min/mean/med)	<100
$\beta_0$	7190/11515/12169	0%	5947/11086/11811	0%	3813/9060/9387	0%
$\beta_1$	6403/11032/11721	0%	5245/10666/11359	0%	3306/8532/8761	0%
$\Lambda$	146/1683/234	0%	509/4817/2773	0%	125/299/154	0%
$F$	366/9070/10396	0%	3355/13500/14279	0%	308/7077/5312	0%
$\Sigma$	6299/10914/12264	0%	5965/11272/12648	0%	4239/9601/11133	0%

Table 4: Comparison of effective sample size (ESS)—reported as minimum, mean, and median, and the proportion of variables with low ESS values ( $ESS < 100$ )— across three sensitivity tests. Results are shown for the intercepts  $\beta_0$ , regression coefficients  $\beta_1$ , loading matrix  $\Lambda$ , matrix of latent factors  $F$ , and the noise covariance matrix  $\Sigma$ , based on MCMC chains of 20,000 iterations with the first 5,000 iterations discarded as warm-up.

	Test 1		Test 2		Test 3	
	Eucl. Dist.	Sphere Var.	Eucl. Dist.	Sphere Var.	Eucl. Dist.	Sphere Var.
$f_1$	0.3446	0.0574	0.5843	0.0488	0.3221	0.1279
$f_2$	0.4377	0.1569	0.6923	0.1093	0.4133	0.147

Table 5: Comparison of posterior summaries for the two latent spatial factors ( $f_1$  and  $f_2$ ) across three sensitivity tests. Each test is evaluated using two diagnostics: Euclidean distance between the true and estimated factor, and the spherical variance of the posterior samples.

Specifically, Test 2, which imposed priors misaligned with the true factor smoothness, yielded the most stable MCMC chains for  $\Lambda$  and  $F$  (highest ESS overall) and the lowest spherical variances, indicating highly concentrated posterior samples. However, this stability was achieved at the expense of accuracy; Test 2 exhibited the largest Euclidean distances between the estimated and true factors. The visual results in Figure 4 corroborate this, showing noticeable oversmoothing in the estimated  $f_2$  for Test 2 compared to the true pattern and the estimates from the other tests. Conversely, Test 3, employing weaker priors, resulted in generally lower ESS values but achieved Euclidean distances comparable to or better than Test 1. This suggests that relaxed prior constraints can improve factor recovery accuracy by mitigating prior-induced bias, despite potentially lower sampling efficiency.

## 6. REAL DATA ANALYSIS

The application and utility of the proposed BSF model sampled through ProjMC<sup>2</sup> are illustrated using a spatial transcriptomics (ST) dataset. As a probabilistic regression framework, the model facilitates comprehensive posterior inference for all parameters, enabling an interpretable analysis of spatial transcriptomics

---

data. This is particularly valuable for exploring spatial patterns in novel datasets lacking annotations or benchmarks. This analysis used a public 10x Genomics Xenium healthy human kidney dataset 10x Genomics (2024), profiling the expression of the Xenium Human Multi-Tissue and Cancer Panel (377 genes) across 97,560 cells. An initial filter retained cells with detectable expression for at least 20 genes, resulting in a final dataset comprising 69,490 cells for analysis. The Hematoxylin and Eosin stained tissue image is in Figure 5(a). Gene expression counts were normalized using the `SCTransform` function in the Seurat R package.

The BSF model was fitted with  $K = 6$  latent factors (embeddings). Priors for regression coefficients ( $\beta$ ), factor loadings ( $\Lambda$ ), and error covariance ( $\Sigma$ ) were specified identically to those for the simulation studies. Spatial decay parameters for the six factors were selected from a discrete grid, allowing effective spatial ranges to vary between 2000 and 600 micrometers. A single MCMC chain was run for 1000 iterations, discarding the initial 500 iterations as burn-in. ESS diagnostics (500 post-burn-in samples) indicated satisfactory convergence for spatial factors  $\mathbf{F}$  (only 209 of 416,940 elements had ESS < 100). Posterior mean of the latent factors, scaled by the norm of the corresponding row in the estimated loading matrix ( $\hat{\Lambda}$ ), were extracted as low-dimensional spatial embeddings for downstream analyses. The posterior mean of the product  $\mathbf{F}\hat{\Lambda}$  was computed to represent the estimated spatially varying component of gene expression, effectively denoised and centered.

For comparison, alternative dimension reduction and clustering techniques were applied to the same filtered and normalized dataset. These included Principal Component Analysis (PCA), using the top 18 principal components (selected via elbow plot) for subsequent clustering, and two contemporary graph-based methods for spatial transcriptomics: STAGATE (Dong and Zhang, 2022) and GraphST (Long et al., 2023), identified as representative in recent benchmarks (Kang et al., 2025). Default parameter settings were used to obtain low-dimensional embeddings from STAGATE and GraphST.

To identify distinct spatial domains (clusters), Gaussian mixture models (`mclust` R package) were applied to the low-dimensional embeddings from all methods, identifying 8 distinct clusters. The BSF result is visualized in Figure 5 (b). To facilitate a closer comparison of clustering performance, focus was placed on a subregion exhibiting rich spatial heterogeneity (indicated by the black circle in Figure 5 (b)). Clustering results within this subregion for PCA, STAGATE, GraphST, and BSF are displayed in Figure 5 (c-f). Qualitatively, PCA yielded the most fragmented clustering, albeit capturing some large-scale spatial trends. STAGATE produced clusters with well-defined boundaries and relatively simple structures. The spatial domains identified by GraphST and BSF appear more structurally similar. However, definitive evaluation is challenging due to the absence of ground-truth annotations. To elucidate the biological basis of the BSF-identified clusters, the dominant gene expression patterns contributing to the estimated spatial

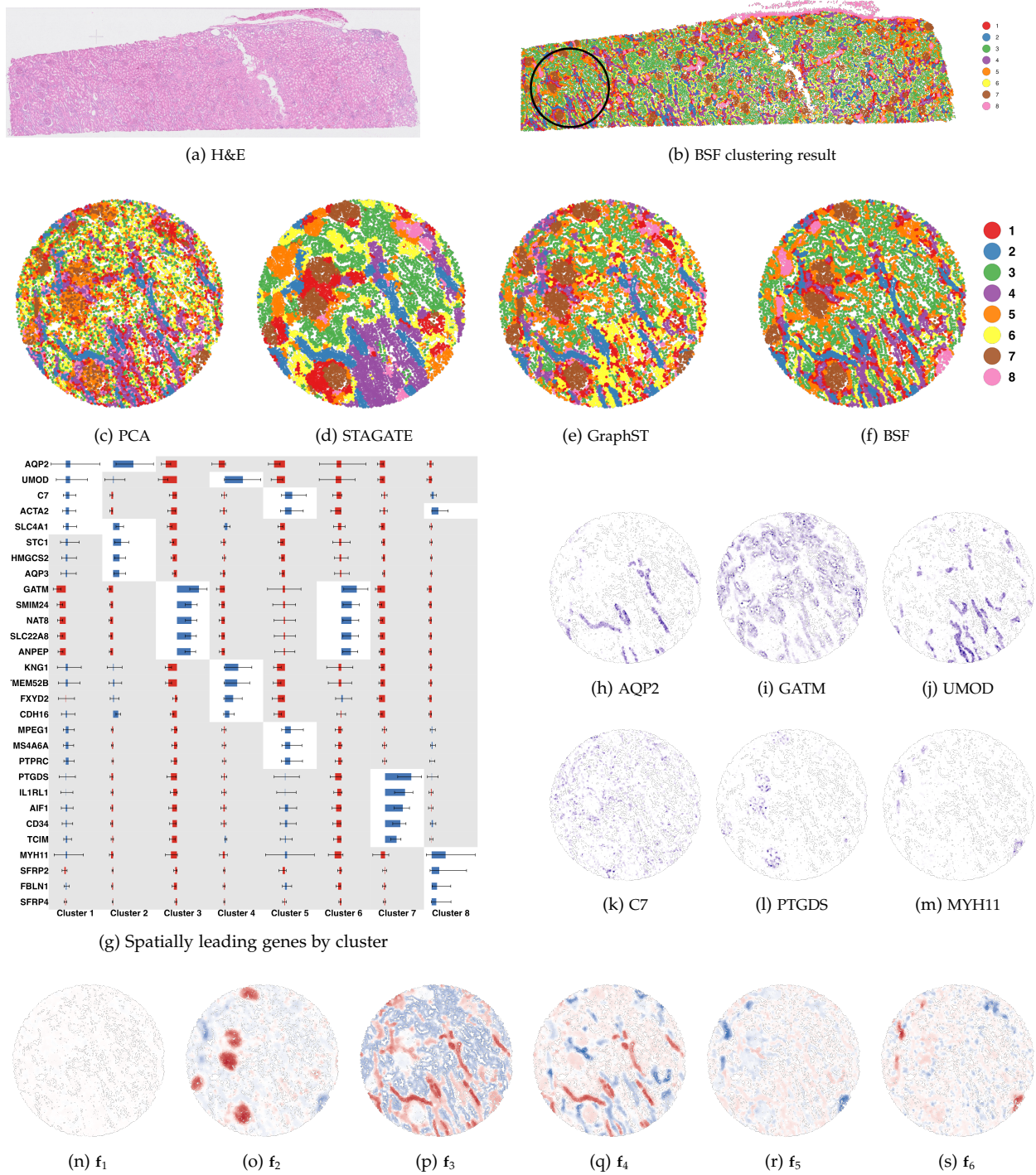


**Figure 5: Spatial Transcriptomics of a Human Kidney Section: Clustering, Marker Genes, and Latent Factor Patterns** (a) H&E-stained image of a Xenium-captured kidney section. (b) Unsupervised clustering on the whole tissue using posterior means of BSF spatial factors; region of interest highlighted by a black circle. (c–f) Clustering within the region of interest via PCA (c), STAGATE (d), GraphST (e), and BSF (f), using *mclust* with 8 clusters. (g) Top cluster-specific spatially variable genes identified by BSF, based on posterior means of FA; Each bar plot shows the distribution (mean and 90% CI) of spatial effects (beyond intercept and noise) across all cells within the cluster. (h–m) Spatial expression patterns of representative marker genes (AQP2, GATM, UMOD, C7, PTGDS, MYH11) selected based on their prominence in panel (g). (n–s) Spatial pattern of six latent spatial factors ( $f_1$ – $f_6$ ) estimated by BSF in the selected region.

---

random effects (posterior mean of  $\mathbf{FA}$ ) were investigated. For each of the 8 clusters, genes were ranked based on their mean estimated spatial effect, and the top five contributing genes were selected. Figure 5 (g) presents the distributions (mean and 90% credible intervals) of these estimated gene-specific spatial effects for the leading genes per cluster. This methodology isolates spatially structured gene expression signals from non-spatial variation and noise, yielding more interpretable molecular signatures for each spatial domain and informing the selection of representative marker genes visualized in Figure 5 (h–m).

Based on the cluster-specific gene signatures summarized in Figure 5 (g) and the spatial expression patterns in Figure 5 (h–m), potential biological identities for several clusters can be inferred. Cluster 2 is characterized by high AQP2 expression (Figure 5 (h)), suggesting collecting ducts. Cluster 3 shows elevated GATM expression (Figure 5 (i)), indicative of proximal tubule regions. Cluster 4 exhibits strong UMOD expression (Figure 5 (j)), characteristic of the thick ascending limb. Cluster 7 displays high PTGDS expression (Figure 5 (l)) and a morphology consistent with glomeruli. Other clusters (1, 5, 6, 8) appear less distinct, either lacking a single dominant marker gene or exhibiting expression profiles similar to adjacent clusters (Figure 5 (g)). These often correspond to boundary regions between major anatomical structures. Finally, Figure 5 (n–s) visualizes the spatial patterns of the six estimated latent factors ( $\mathbf{f}_1, \dots, \mathbf{f}_6$ ) in the subregion, each capturing distinct, smooth spatial gene expression structures that delineate clustered tissue domains.

This application highlights several key advantages of the proposed BSF model. First, the explicit modeling of spatial dependence through latent factors allows BSF to effectively capture and represent smooth spatial patterns inherent in the tissue architecture (Figure 5 (n–s)). This spatial smoothing contributes to denoising the expression data, facilitating the identification of biologically relevant domains. Second, the resulting low-dimensional embeddings and estimated spatial effects ( $\mathbf{FA}$ ) provide interpretable summaries of complex ST data. Compared to PCA, the BSF embeddings lead to more spatially coherent clusters (Figure 5 (c) vs 5 (f)). While graph-based methods like STAGATE and GraphST also produce structured clusters, BSF offers the additional benefits of a generative model, including posterior inference and the direct estimation of spatially varying gene contributions (Figure 5 (g)). The ability to identify marker genes based on modeled spatial effects, rather than just overall expression levels, provides a powerful tool for interpreting the biological significance of the discovered spatial domains. Thirdly, its probabilistic nature provides a principled framework for uncertainty quantification. The model can provide full posterior distributions not only for the spatial effects of specific genes within identified clusters but also for factor loadings and other model parameters, allowing for the potential incorporation of prior information and offering richer insights than point estimates alone. Computationally, on a MacBook Pro (M2 Max chip, no NVIDIA GPU), STAGATE required 1 hour 35 minutes and GraphST 3 hours 36 minutes. The BSF

---

MCMC (1000 iterations) completed in 5 hours 8 minutes. However, convergence diagnostics suggest the MCMC chain could potentially have been terminated earlier with satisfactory ESS. Although MCMC-based inference is more computationally intensive, the runtime remains manageable for datasets of this scale. The substantial benefits in model interpretability, principled uncertainty quantification, and direct spatial dependency modeling justify the computational investment.

## 7. CONCLUSION AND FUTURE WORK

This paper proposed the ProjMC<sup>2</sup> algorithm for scalable Bayesian spatial factor models. Unlike traditional approaches relying on explicit posterior distributions, ProjMC<sup>2</sup> defines the target distribution implicitly via conditional distributions and a projection step, ensuring convergence through an existence proof. Simulations confirm enhanced convergence, mixing, and identifiability of latent factors and loadings. The inherent QR decomposition naturally orders latent factors without constraining likelihood. ProjMC<sup>2</sup> readily extends to multi-slice spatial transcriptomics (ST) data, combining outcomes and design matrices from multiple slices. Incorporating slice-specific indicators allows effective estimation and correction of inter-slice variability, improving inference robustness. Future extensions include integrating sparsity-inducing priors (e.g., spike-and-slab, Horseshoe) for gene selection, and adapting the framework for spatio-temporal and environmental exposure analyses. While the domain of low-dimensional embedding and pattern recognition is increasingly dominated by auto-encoder-based ‘black-box’ algorithms, a compelling case remains for principled, regression-based modeling. The pursuit of understanding and elucidating underlying mechanisms is a cornerstone of scientific inquiry, enabling the translation of knowledge into actionable insights. This work underscores the continued relevance and utility of interpretable statistical models in this endeavor.

## 8. ACKNOWLEDGMENTS

This work was supported by the National Institutes of Health (NIH) under Grant P20HL176204, P30ES007048, and R01ES031590. Special thanks to Kelly N Street, Jesse A Goodrich, and Jonathan Nelson for their fruitful discussions on applications.

## REFERENCES

10x Genomics (2024). “Human Kidney Preview Data - Xenium Human Multi-Tissue and Cancer Panel 1 Standard.” <https://www.10xgenomics.com/datasets/>

- 
- human-kidney-preview-data-xenium-human-multi-tissue-and-cancer-panel-1-standard. Accessed: 2025-04-28.
- Banerjee, S., Carlin, B. P., and Gelfand, A. E. (2014). *Hierarchical modeling and analysis for spatial data*. CRC Press, Boca Raton, FL.
- Banerjee, S., Gelfand, A. E., Finley, A. O., and Sang, H. (2008). "Gaussian Predictive Process Models for Large Spatial Datasets." *Journal of the Royal Statistical Society, Series B*, 70: 825–848.
- Bentley, J. L. (1975). "Multidimensional binary search trees used for associative searching." *Communications of the ACM*, 18(9): 509–517.
- Bressan, D., Battistoni, G., and Hannon, G. J. (2023). "The dawn of spatial omics." *Science*, 381(6657): eabq4964.
- Chakraborty, R. and Vemuri, B. C. (2019). "Statistics on the Stiefel manifold: Theory and applications."
- Cressie, N. and Wikle, C. K. (2015). *Statistics for spatio-temporal data*. John Wiley & Sons, Hoboken, NJ.
- Dai, T., Dai, Q., Yin, J., Chen, J., Liu, B., Bi, X., Wu, J., Zhang, Y., and Feng, Y. (2024). "Spatial source apportionment of airborne coarse particulate matter using PMF-Bayesian receptor model." *Science of The Total Environment*, 917: 170235.
- Datta, A., Banerjee, S., Finley, A. O., and Gelfand, A. E. (2016). "Hierarchical nearest-neighbor Gaussian process models for large geostatistical datasets." *Journal of the American Statistical Association*, 111: 800–812.
- Dawid, A. P. (1981). "Some matrix-variate distribution theory: Notational considerations and a Bayesian application." *Biometrika*, 68(1): 265–274.
- Dong, K. and Zhang, S. (2022). "Deciphering spatial domains from spatially resolved transcriptomics with an adaptive graph attention auto-encoder." *Nature communications*, 13(1): 1739.
- Du, J., Zhang, H., and Mandrekar, V. S. (2009). "Fixed-domain asymptotic properties of tapered maximum likelihood estimators." *The Annals of Statistics*, 37(6A): 3330–3361.
- Finley, A. O., Datta, A., Cook, B. C., Morton, D. C., Andersen, H. E., and Banerjee, S. (2019). "Efficient algorithms for Bayesian Nearest Neighbor Gaussian Processes." *Journal of Computational and Graphical Statistics*, 28(2): 401–414.
- Finley, A. O., Sang, H., Banerjee, S., and Gelfand, A. E. (2009). "Improving the performance of predictive process modeling for large datasets." *Computational statistics and data analysis*, 53(8): 2873–2884.

- 
- Fong, D. C.-L. and Saunders, M. (2011). "LSMR: An iterative algorithm for sparse least-squares problems." *SIAM Journal on Scientific Computing*, 33(5): 2950–2971.
- Gelman, A., Carlin, J. B., Stern, H. S., Dunson, D. B., Vehtari, A., and Rubin, D. B. (2013). *Bayesian Data Analysis, 3rd Edition*. Chapman & Hall/CRC Texts in Statistical Science. Chapman & Hall/CRC.
- Golub, G. H. and Van Loan, C. F. (2012). *Matrix Computations, 4th Edition*. Johns Hopkins University Press.
- Guinness, J. (2018). "Permutation and grouping methods for sharpening Gaussian process approximations." *Technometrics*, 60(4): 415–429.
- Halko, N., Martinsson, P.-G., Shkolnisky, Y., and Tygert, M. (2011). "An algorithm for the principal component analysis of large data sets." *SIAM Journal on Scientific computing*, 33(5): 2580–2594.
- Kang, L., Zhang, Q., Qian, F., Liang, J., and Wu, X. (2025). "Benchmarking computational methods for detecting spatial domains and domain-specific spatially variable genes from spatial transcriptomics data." *Nucleic Acids Research*, 53(7): gkaf303.
- Katzfuss, M. and Guinness, J. (2021). "A general framework for Vecchia approximations of Gaussian processes." *Statistical Science*, 36(1): 124–141.
- Lee, Y., Lee, M., Shin, Y., Kim, K., and Kim, T. (2025). "Spatial Omics in Clinical Research: A Comprehensive Review of Technologies and Guidelines for Applications." *International Journal of Molecular Sciences*, 26(9): 3949.
- Long, Y., Ang, K. S., Li, M., Chong, K. L. K., Sethi, R., Zhong, C., Xu, H., Ong, Z., Sachaphibulkij, K., Chen, A., et al. (2023). "Spatially informed clustering, integration, and deconvolution of spatial transcriptomics with GraphST." *Nature Communications*, 14(1): 1155.
- Lopes, H. F., Salazar, E., and Gamerman, D. (2008). "Spatial Dynamic Factor Analysis." *Bayesian Analysis*, 3(4): 759 – 792.
- Mardia, K. V. and Jupp, P. E. (2009). *Directional statistics*. John Wiley & Sons.
- Martinsson, P.-G. and Tropp, J. A. (2020). "Randomized numerical linear algebra: Foundations and algorithms." *Acta Numerica*, 29: 403–572.
- Matérn, B. (1986). *Spatial Variation*. Springer-Verlag.
- Meyn, S. P. and Tweedie, R. L. (2012). *Markov chains and stochastic stability*. Springer Science & Business Media.



- 
- Moses, L. and Pachter, L. (2022). “Museum of spatial transcriptomics.” *Nature methods*, 19(5): 534–546.
- Nishimura, A. and Suchard, M. A. (2023). “Prior-preconditioned conjugate gradient method for accelerated Gibbs sampling in “large n, large p” Bayesian sparse regression.” *Journal of the American Statistical Association*, 118(544): 2468–2481.
- Ren, Q. and Banerjee, S. (2013). “Hierarchical factor models for large spatially misaligned datasets: A low-rank predictive process approach.” *Biometrics*, 69: 19–30.
- Robert, C. P., Casella, G., and Casella, G. (1999). *Monte Carlo statistical methods*, volume 2. Springer.
- Schäfer, F., Katzfuss, M., and Owhadi, H. (2021). “Sparse Cholesky Factorization by Kullback–Leibler Minimization.” *SIAM Journal on scientific computing*, 43(3): A2019–A2046.
- Shang, L. and Zhou, X. (2022). “Spatially aware dimension reduction for spatial transcriptomics.” *Nature communications*, 13(1): 7203.
- Song, Y., Li, H., Li, J., Mao, C., Ji, J., Yuan, X., Li, T., Ayoko, G. A., Frost, R. L., and Feng, Y. (2018). “Multivariate linear regression model for source apportionment and health risk assessment of heavy metals from different environmental media.” *Ecotoxicology and Environmental Safety*, 165: 555–563.
- Stein, M. L. (1999). *Interpolation of Spatial Data: Some Theory for Kriging*. Springer, first edition.
- (2014). “Limitations on Low Rank Approximations for Covariance Matrices of Spatial Data.” *Spatial Statistics*, 8(0): 1–19.
- Stephens, M. (2000). “Dealing with label switching in mixture models.” *Journal of the Royal Statistical Society: Series B (Statistical Methodology)*, 62(4): 795–809.
- Tang, W., Zhang, L., and Banerjee, S. (2021). “On identifiability and consistency of the nugget in Gaussian spatial process models.” *Journal of the Royal Statistical Society Series B: Statistical Methodology*, 83(5): 1044–1070.
- Taylor-Rodriguez, D., Finley, A. O., Datta, A., Babcock, C., Andersen, H. E., Cook, B. D., Morton, D. C., and Banerjee, S. (2019). “Spatial factor models for high-dimensional and large spatial data: An application in forest variable mapping.” *Statistica Sinica*, 29(3): 1155–1180.
- Titsias, M. (2009). “Variational learning of inducing variables in sparse Gaussian processes.” In *Artificial intelligence and statistics*, 567–574. PMLR.

- 
- Townes, F. W. and Engelhardt, B. E. (2023). "Nonnegative spatial factorization applied to spatial genomics." *Nature methods*, 20(2): 229–238.
- Velten, B., Braunger, J. M., Argelaguet, R., Arnol, D., Wirbel, J., Bredikhin, D., Zeller, G., and Stegle, O. (2022). "Identifying temporal and spatial patterns of variation from multimodal data using MEFISTO." *Nature methods*, 19(2): 179–186.
- Wang, F. and Wall, M. M. (2003). "Generalized common spatial factor model." *Biostatistics*, 4(4): 569–582.
- Zhang, H. (2004). "Inconsistent estimation and asymptotically equal interpolations in model-based geostatistics." *Journal of the American Statistical Association*, 99(465): 250–261.
- Zhang, H. and Zimmerman, D. L. (2005). "Towards reconciling two asymptotic frameworks in spatial statistics." *Biometrika*, 92(4): 921–936.
- Zhang, L. (2022). "Applications of Conjugate Gradient in Bayesian Computation." *Wiley StatsRef: Statistics Reference Online*, 1–7.
- Zhang, L. and Banerjee, S. (2022). "Spatial factor modeling: A Bayesian matrix-normal approach for misaligned data." *Biometrics*, 78(2): 560–573.
- Zhang, L., Datta, A., and Banerjee, S. (2019). "Practical Bayesian Modeling and Inference for Massive Spatial Datasets On Modest Computing Environments." *Statistical Analysis and Data Mining: The ASA Data Science Journal*, 12(3): 197–209.
- Zhang, L., Tang, W., and Banerjee, S. (2024). "Fixed-domain asymptotics under Vecchia's approximation of spatial process likelihoods." *Statistica Sinica*, 34(4): 1863.

## S.1. ALGORITHM OF NNGP BASED BLMC MODEL

---

**Algorithm 1:** ProjMC<sup>2</sup> for NNGP based BSF model with diagonal  $\Sigma$

---

1. **Input:** Design matrix  $\mathbf{X}$ , outcomes  $\mathbf{Y}$ , set of spots  $\chi$ , prior parameters  $\mu_\beta, \mathbf{V}_\beta, \mu_\Lambda, \mathbf{V}_\Lambda, a, \{b_i, i = 1, \dots, q\}$ , prefixed parameters  $\{\psi_k, k = 1, \dots, K\}$ , number of MCMC iterations  $L$  and iterations for warm-up  $L_{warm}$ .
2. Precalculation
  - (a) Construct the maximin ordering of  $\chi$   $\mathcal{O}(n \log(n))$
  - (b) Build the nearest neighbor for  $S$  with the new ordering using K-D tree (Bentley, 1975)  $\mathcal{O}(n \log(n))$
  - (c) Calculate Cholesky decompositions  $\mathbf{V}_\Lambda = \mathbf{L}_\Lambda \mathbf{L}_\Lambda^\top$  and  $\mathbf{V}_\beta = \mathbf{L}_\beta \mathbf{L}_\beta^\top$   $\mathcal{O}(p^3 + K^3)$
  - (d) Construct  $\{\mathbf{A}_{\rho_k}\}_{k=1}^K$  and  $\{\mathbf{D}_{\rho_k}\}_{k=1}^K$  as described, for example, in Finley et al. (2019)  $\mathcal{O}(Knm^3)$
3. Pre-allocation
  - (a) Pre-allocation for MCMC chains storage:  $\mathcal{O}(L \cdot \{nK + (p + K) \cdot q + q\})$
  - (b) Pre-allocation for  $\beta, \Lambda$  and  $\Sigma$  update:  $\mathbf{X}^*, \mathbf{Y}^*, \mu^*, \mathbf{L}^*$  the Cholesky decomposition of  $\mathbf{V}^*$ , storage:  $\mathcal{O}(nq)$   
vector  $\mathbf{u}$  with length  $(p + K)q$ , matrix for storing residual  $\mathbf{Y}_{\chi m} = \mathbf{Y}^* - \mathbf{X}^* \mu^*$ , and vector for storing updated  $b^*$  for all outcomes.
  - (c) Pre-allocation for  $\tilde{\mathbf{F}}$  update:  $\tilde{\mathbf{X}}, \tilde{\mathbf{Y}}, \mathbf{F}$ , QR decomposition of  $\mathbf{F}$ , diagonal matrix  $D_\Sigma$ , storage:  $\mathcal{O}(nq)$   
 $f_m$  that store column mean of  $\mathbf{F}$ , and vector  $\mathbf{v}$  with length  $n(K + q)$ .
4. Initialization
  - (a)  $\beta^{(0)} = (\mathbf{X}^\top \mathbf{X})^{-1} \mathbf{X}^\top \mathbf{Y}$   $\mathcal{O}(np^2 + npq)$
  - (b) Conduct randomized SVD of  $\mathbf{R} = \mathbf{Y} - \mathbf{X}\beta$  with  $K$  principle components, store the loading matrix as  $\Lambda^{(0)}$  and update remaining residual  $\mathbf{R}$   $\mathcal{O}(nqK)$
  - (c) For  $i = 1, \dots, q$ , initialize  $\sigma_i^{2(0)}$  with variance of the the remaining residual.  $\mathcal{O}(nq)$
5. Projected MCMC sampling. For  $l = 1 : L$ 
  - (a) Update  $\mathbf{F}^{(l)}$ 
    - Update  $\tilde{\mathbf{X}}$  and  $\tilde{\mathbf{Y}}$  in (2.6)
      - For  $l = 1$ , initialize  $\tilde{\mathbf{Y}}$  and  $\tilde{\mathbf{X}}$  in (2.6) with  $\mathbf{L}_k^{-1} = \mathbf{D}_{\rho_k}^{-\frac{1}{2}} (\mathbf{I} - \mathbf{A}_{\rho_k})$ .  $\mathcal{O}(nq(p + K) + nmK) \approx \mathcal{O}(nq)$
      - Update  $D_\Sigma$  with diagonal elements from  $\Sigma^{(l-1)}$   $\mathcal{O}(q)$
      - Update  $\tilde{\mathbf{X}}$  and  $\tilde{\mathbf{Y}}$  in (2.6) with  $\Sigma = D_\Sigma$ ,  $\beta = \beta^{(l-1)}$  and  $\Lambda = \Lambda^{(l-1)}$ .  $\mathcal{O}((p + K)nq)$
    - Use LSMR (Fong and Saunders, 2011) to generate sample of  $\mathbf{F}^{(l)}$ 
      - Sample  $\mathbf{v} \sim \mathcal{N}(\mathbf{0}, \mathbf{I}_{Kn})$   $\mathcal{O}(nK)$
      - Solve  $\text{vec}(\mathbf{F})$  from  $\tilde{\mathbf{X}} \text{vec}(\mathbf{F}) = \tilde{\mathbf{Y}} + \mathbf{v}$  by LSMR
  - (b) Generate projected embeddings  $\tilde{\mathbf{F}}^{(l)} = g(\mathbf{F}^{(l)})$ 
    - Record column mean of  $\mathbf{F}$  in  $f_m$  and update  $\mathbf{F} = \mathbf{F} - \mathbf{1}_n f_m^\top$   $\mathcal{O}(nq)$
    - Compute the thin Q matrix of  $\mathbf{F}$  using Modified Gram-Schmidt (MGS) and store it as  $\tilde{\mathbf{F}}$   $\mathcal{O}(nK^2)$
    - update  $\tilde{\mathbf{F}} = \sqrt{n} \cdot \mathbf{Q}$   $\mathcal{O}(nK)$
  - (c) Use MNIW to update  $\{\beta^{(l)}, \Lambda^{(l)}, \Sigma^{(l)}\}$ 
    - Construct  $\mathbf{X}^*$  and  $\mathbf{Y}^*$  in (2.5) with  $\mathbf{F}$  replaced by  $\tilde{\mathbf{F}}^{(l)}$

- 
- Calculate the Cholesky decomposition  $\mathbf{L}^*$  of  $\mathbf{V}^{*-1} = \mathbf{X}^{*\top} \mathbf{X}^* = \mathbf{L}^* \mathbf{L}^{*\top}$ .  $\mathcal{O}((n+p+K)(p+K)^2)$
  - Calculate  $\boldsymbol{\mu}^* = \mathbf{V}^* [\mathbf{X}^{*\top} \mathbf{Y}^*]$  and update  $\mathbf{Y}_{Xm} = \mathbf{Y}^* - \mathbf{X}^* \boldsymbol{\mu}^*$   $\mathcal{O}((n+p+K)(p+K)q)$
  - Compute  $b_i^*$  and sample elements of  $\boldsymbol{\Sigma}^{(l)}$  from Inverse-Gamma with parameters provided in (4.1)  $\mathcal{O}((n+p+K)q)$
  - Sample  $\boldsymbol{\gamma}^{(l)} = [\boldsymbol{\beta}^{(l)\top}, \boldsymbol{\Lambda}^{(l)\top}]^\top$  from  $\text{MN}(\boldsymbol{\mu}^*, \mathbf{V}^*, \boldsymbol{\Sigma}^{(l)})$ 
    - i. Sample  $\mathbf{u} \sim \text{MN}(\mathbf{0}, \mathbf{I}_{p+K}, \{\boldsymbol{\Sigma}^{(l)}\}^{1/2})$   $\mathcal{O}((p+K)q)$
    - ii. Generate  $\boldsymbol{\gamma}^{(l)} = \boldsymbol{\mu}^* + \mathbf{L}^{*- \top} \mathbf{u}$   $\mathcal{O}((p+K)^2 q)$
6. **Output:** Posterior samples  $\{\hat{\mathbf{F}}^{(l)}, \boldsymbol{\beta}^{(l)}, \boldsymbol{\Lambda}^{(l)}\}_{l=1, \dots, L}$  of low-dimensional embeddings, regression coefficients, and loading matrix.
- 

## S.2. VALUES OF PARAMETERS IN SIMULATION EXAMPLES

### S.2.1. Values of parameters to generate simulations in simulation example 1

$$\begin{aligned}
 \boldsymbol{\beta} &= \begin{bmatrix} 1.0 & -1.0 & 1.0 & -0.5 & 2.0 & -1.5 & 0.5 & 0.3 & -2.0 & 1.5 \\ -3.0 & 2.0 & 2.0 & -1.0 & -4.0 & 3.0 & 4.0 & -2.5 & 5.0 & -3.0 \end{bmatrix} \\
 \boldsymbol{\Lambda} &= \begin{bmatrix} 0.81 & 0.49 & -0.49 & -0.15 & -0.8 & 0.38 & -0.94 & 0.86 & 0.16 & -0.76 \\ -0.11 & 0.02 & -0.33 & 0.74 & -0.75 & -0.73 & -0.3 & 0.92 & -0.38 & -0.59 \end{bmatrix} \\
 \text{Diagonal}(\boldsymbol{\Sigma}) &= \begin{bmatrix} 0.5 & 1 & 0.4 & 2 & 0.3 & 2.5 & 3.5 & 0.45 & 1.5 & 0.5 \end{bmatrix}
 \end{aligned}$$

$$\phi_1 = 6.0, \phi_2 = 9.0$$